MASARYKOVA UNIVERZITA
PŘÍRODOVĚDECKÁ FAKULTA
ÚSTAV TEORETICKÉ FYZIKY A ASTROFYZIKY

DIPLOMOVÁ PRÁCE

Studium rentgenového záření z blízkosti černých děr

Vladimír Domček

Vedoucí diplomové práce:
RNDr. Jiří Svoboda, Ph.D.

Brno 2016

Bibliografický záznam

Autor: Vladimír Domček
Přírodovědecká fakulta, Masarykova univerzita
Ústav teoretické fyziky a astrofyziky

Název práce: Studium rentgenového záření z blízkosti černých děr

Studijní program: Fyzika

Studijní obor: Teoretická fyzika a astrofyzika

Vedoucí práce: RNDr. Jiří Svoboda, Ph.D.

Akademický rok: 2015/16

Počet stran: 7+67

Klíčová slova: rentgenová spektroskopie, černé díry, aktivní galaktická jádra:NGC 985, warm absorber

Bibliographic entry

Author:	Vladimír Domček Faculty of Science, Masaryk University Department of Theoretical Physics and Astrophysics
Title of thesis:	X-Ray Radiation from the Innermost Regions around Black Holes
Degree Programme:	Physics
Field of Study:	Theoretical physics and astrophysics
Supervisor:	RNDr. Jiří Svoboda, Ph.D.
Academic Year:	2015/16
Number of Pages:	7+67
Keywords:	X-ray spectroscopy, black holes, active galactic nuclei:NGC 985, warm absorber

Abstrakt

Aktivní galaktická jádra jsou kompaktní oblasti v centrech galaxií, které produkují záření na různých vlnových délkách, od rádiového oboru přes ultrafialovou a rentgenovou část spektra až po záření gamma. Nejenergetičtější záření pochází z nejvnitřnějších oblastí a předpokládá se o něm, že pochází z tzv. akrece, tedy postupného dopadu hmoty, na super-hmotnou černou díru.

V první části práce studujeme jeden z otevřených problémů rentgenové spektroskopie černých děr, měření strmých hodnot radiálního profilu emisivity odraženého rentgenového záření z povrchu akrečního disku. Systematicky zkoumáme, jak jsou měření radiální emisivity ovlivněny různými předpoklady o ionizačním profilu disku v důsledku různé hustoty a ozáření rentgenovým zdrojem. Výsledky ukazujeme pro tři nejčastěji používané modely, a to na simulovaných datech tří různých současných i plánovaných rentgenových misí.

Druhá část práce shrnuje výsledky analýzy rentgenových dat Seyfertovy galaxie typu 1 NGC 985, pozorované největší rentgenovou observatoří ESA, družicí XMM-Newton. V naší práci analyzujeme vysoce rozlišená spektra za účelem modelování vytékajícího částečně ionizovaného plynu (tzv. warm absorber). Zkoumáme fyzikální vlastnosti tohoto plynu, především určujeme sloupcovou hustotu vodíku, úrovně ionizace a rychlosti výtoku plynu, a dále studujeme, jak tyto vlastnosti reagují s ohledem na nově objevený probíhající zákryt.

Klíčová slova: rentgenová spektroskopie, černé díry, aktivní galaktická jádra:NGC 985, warm absorber

Abstract

Active Galactic Nuclei are compact regions at the center of galaxies that produce emission in a variety of wavelengths, from the radio through UV, X-ray up until energetic Gamma-ray. The most energetic radiation comes from the innermost parts of this objects and is believed to be produced by accretion of matter onto a supermassive black hole.

In the first part of our work we study one of the open problems of black hole X-ray spectroscopy, the measurement of the steep radial-emissivity profile of the X-ray reflection emission from the accretion disc. We systematically explore how the radial emissivity measurements are affected by different assumptions about the ionisation profile due to different density and X-ray illumination of the accretion disc. We also show variations between three most commonly used models and simulate the data for three different current and planned X-ray missions.

The second part of this thesis summarises the analysis of X-ray data of the Seyfer 1 galaxy NGC 985, observed by ESA's largest X-ray observatory. In our study, we analyse high-resolution spectra to model outflowing partially ionised gas, the so-called Warm Absorbers. We examine the physical properties of the warm absorber, in particular we constrain column densities of hydrogen, levels of ionisation and outflowing velocities of the gas and how they respond to the newly discovered occurring eclipsing event.

Keywords: X-ray spectroscopy, black holes, active galactic nuclei:NGC 985, warm absorber

Masarykova univerzita

Přírodovědecká fakulta

ZADÁNÍ DIPLOMOVÉ PRÁCE

Student   : **Bc. Vladimír Domček, učo <u>394013</u>**

Studijní program : **Fyzika**

Studijní obor   : **Teoretická fyzika a astrofyzika**

Ředitel Ústavu teoretické fyziky a astrofyziky PřF MU Vám ve smyslu Studijního a zkušebního řádu MU určuje diplomovou práci s tématem:

Studium rentgenového záření z blízkosti černých děr

X-Ray Radiation from the Innermost Regions around Black Holes

Zásady pro vypracování: Akrece hmoty na černé díry je zdrojem velmi energetického záření, k jehož uvolňování dochází v jádrech aktivních galaxií, případně u rentgenových dvojhvězd. Toto záření se nejvíce projevuje v rentgenovém oboru, ve kterém jsou tyto zdroje nejsvítivějšími pozorovanými objekty ve vesmíru. Přestože jsou tyto objekty intenzivně studovány od samého zrodu velkých rentgenových laboratoří, stále neznáme zcela přesně mechanismy uvolňování energie akrečními procesy. Předmětem této diplomové práce bude studium rentgenového záření pocházejícího z těchto zdrojů s využitím nejnovějších modelů a observačních dat.

Seznam literatury:
Truemper J., Hasinger G. (Eds.), 2008, The Universe in X-rays
Reynolds, C. S., 2013, The spin of supermassive black holes, CQGra, 30x, 4004R
Svoboda J. et al., 2012, 545A, 106S
Dovčiak, M.; Karas, V.; Yaqoob, T., 2004, ApJS, 153, 205D
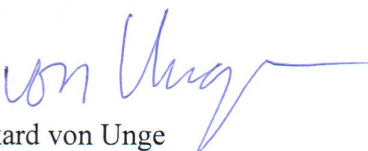HeaSoft package for High Energy Astrophysics, http://heasarc.nasa.gov/lheasoft

Jazyk závěrečné práce   : český, anglický nebo slovenský

Vedoucí diplomové práce   : RNDr. Jiří Svoboda, Ph.D.

Datum zadání diplomové práce   : leden 2015

Datum odevzdání diplomové práce : dle harmonogramu ak. roku 2015/2016

V Brně leden 2015   Rikard von Unge

                                         ředitel ÚTFA

Zadání diplomové práce převzal dne: Podpis studenta

Acknowledgements

My greatest and sincerest Thank you belongs to my supervisor RNDr. Jiří Svoboda, Ph.D. I appreciate his valuable advice, support and patience with me. He introduced me to the real-world of the science and helped me to be part of it. It was an honour to work with you and I look forward to our future cooperation!

I am also very grateful to my ESAC traineeship supervisors Dr. Jacobo Ebrero and Dr. Maria Santos-Lleó. The time I spent working with them on the project that later became part of my thesis was very rewarding. They were both excellent advisers and this thesis wouldn't be complete without them.

Special thanks belongs to Mgr. Lenka Matěchová for her support and commitment to search for the mistakes in this thesis and to prof. Mgr. Jiří Krtička, Ph.D. for his support from the institute. I am also very thankful to Norbert who lead me to this 'mess'. It was you, who inspired me to work in the high-energy astrophysics and I am not going to forget about that!

I would like to also thank to all my friends, especially Lenka, Ondrej, Zdenek and Jakub for their support and motivation through the studies and Miška for being the beacon of hope when things were hard.

Last but not least, I am very grateful for my dear family, for them believing in me and supporting my every move. I am especially thankful to my grandfather whom I will miss greatly.

Prohlášení

Prohlašuji, že jsem svoji diplomovou práci vypracoval samostatně s využitím informačních zdrojů, které jsou v práci citovány.

Brno 2016 . . . .

Vladimír Domček

Contents

Chapter 1

Introduction

1.1 Active Galactic Nuclei

Active galaxies are objects of the Universe with compact and extremely bright nuclei enclosed inside. These nuclei, also known as Active Galactic Nuclei (short AGN), are usually much smaller than 100 pc (Woltjer 1959). It is a region of the galaxy with several orders of magnitude higher luminosity than the luminosity of the average galaxy such as our own. This release of energy is higher at least at some portion of the spectrum and can't be attributed to any processes known to the stars. However, it is believed, that this energy output can be achieved by an extreme process of accreting matter onto the supermassive black hole. AGNs are divided into several subgroups according to the shape of Spectral Energy Distribution (SED) and observed spectral features. The most general classification divides them by the luminosity of the radio part of the SED to either *radio-quiet* or *radio-loud*. Useful criterium to distinguish them was introduced in the form of radio-optical ratio R_{r-o} of specific fluxes at 6 cm and 440 nm (Kellermann *et al.* 1989). While sources with $R_{r-o} < 1$ are considered radio-quiet, $R_{r-o} > 10$ is clear sign of radio-loud galaxy.

1.1.1 Radio-quiet

Seyfert galaxies

The first systematic study of Seyfert galaxies was performed in 1943 by Carl Seyfert. He selected the list of objects from the plate archives at Mount Wilson Observatory with 'characteristic exceedingly luminous stellar or semi-stellar nucleus' (Seyfert 1943). He studied spectra of 6 active galaxies and found very intense and broad permitted and forbidden lines. The Doppler broadening of some of these emission lines reaches up to 8500 km s^{-1}. In addition majority of these Seyfert galaxies were also classified as spiral.

In the Markarian galaxy survey roughly 10% of all galaxies were recognised as Seyfert galaxies (Longair & Malcolm S. Longair 2011). Later studies by (Khachikian & Weedman 1971, 1974) showed that there are differences between the widths of emission lines in various Seyfert galaxies. They divided them into two main categories.

The first category of the Seyfert galaxies is so-called *Seyfert 1* and includes broad permitted emission lines. Full width of half maximum velocities of these lines reach up to 10 000 km s^{-1}. Mainly, Balmer series of hydrogen, neutral and ionised helium and singly ionised iron are observed. They are also highly variable in the intensity and shape of the profile (Ulrich *et al.* 1984). Apart from the broad permitted lines also much narrower forbidden lines are present in the spectra. Their width reaches velocities of 1 000 km s^{-1}. The second category, *Seyfert 2*, contains both permitted and forbidden emission lines with similar widths of 1 000 km s^{-1}.

Higher quality observations of galaxies NGC 4151 and Markarian 6 later revealed that their spectra contain a superposition of both narrow and broad lines of Balmer series (Osterbrock & Koski 1976). Reflecting on these findings, a further classification was deduced on the relative strength of the components and values of the type started to range between 1 and 2. For example, When broader emission line is stronger than a narrow one, the value of 1.2 could be assigned. It was the first hint that Seyfert galaxies could be unified into one scheme.

Unification of Seyfert galaxies

With further studies, astronomers realised that absorber of a toroidal structure composed of cold dust could be blocking the radiation in Seyfert 2 galaxies. In case of small inclination (the angle between the pole of the galaxy and our line of sight) is small, we observe the source of the radiation directly. We see further into the parts of the galaxy known as the *Broad Line Region* (BLR), where broad lines typical for Seyfert 1's galaxies emerge. When the inclination is high enough, our line of sight goes through the dusty torus that blocks our view of the core. We do not see any broad lines, however, we can still observe narrow lines. They are scattered off the distant clouds in the *Narrow Line Region* (NLR). Visualisation of this geometry is pictured on the bottom side of figure 1.1.

The first demonstration of this unification concept came from the study of Seyfert 2 galaxy NGC 1068 made by (Antonucci & Miller 1985). They observed this close-by galaxy through the high-resolution spectroscopic polarimeter and found the broad Balmer lines and Fe II emission. Moreover, the whole observed polarised spectrum resembled typical spectra of Seyfert 1 galaxies. Their interpretation of these results became later known as standard unification theory of the Seyfert galaxies (Antonucci 1993; Miller 1994).

Even though this simple unification model still stands today, there is an increasing

number of Seyfert 2 AGNs, that does not show any signs of broad lines in the polarimetric studies (Tran 2001, 2003). In a model proposed by Nicastro (2000), these objects might be less luminous and not be able to create BLR. There might be therefore another category of the 'True' Seyfert 2 galaxies that do not fall into this simple unification model of obscuration by the torus. It is one of the open questions in AGN classification and more research will be needed to answer it.

LINERs

After the unification of the Seyfert galaxies, search for their lower luminosity versions started. Soon enough, it was shown that objects with similar spectra but with narrower and weaker emission lines occur (Heckman 1980). These weak active galaxies were named Low Ionisation Nuclear Emission Regions or LINERs and were found out to be quite common. Within 20 to 40 Mpc it was found that approximately one-third of the galaxies displays characteristics of LINERs (Longair & Malcolm S. Longair 2011).

1.1.2 Radio-loud

Quasars

Quasars or 'Quasi-Stellar Objects' were discovered as strong radio sources in first radio surveys like the 3C catalogue (Edge *et al.* 1959). In the process of looking for their optical counterpart on the photographic plates, researchers came across with only something that could be described as a star-like source. Measured spectra of these objects exhibited very broad emission lines of unidentified wavelengths and higher flux in the blue part of the spectrum. The first breakthrough came with Schmidt's realisation, that broad lines were redshifted hydrogen emission lines of Balmer series (Schmidt 1963). He measured the redshift of the source 3C 273 to be $z = 0.158$, one of the highest redshifts measured at that time. The luminosity of the source was calculated to be 100 times larger than typical galaxy such as our own or M31. From that time name of the quasar started to be used.

Few years later, general properties of quasar have been defined. Besides beeing identified as star-like objects with strong radio counterpart, they exhibit also a large UV flux, high variability of the continuum flux and highly redshifted broad emission lines (Schmidt 1969). Radio emission in quasars was found out to be produced by matter moving at relativistic speeds, hence creating synchrotron radiation in the radio bandwidth. From the observations of close-by sources such as 3C 175 (Bridle *et al.* 1993), it was evident that radio emission originated in huge radio lobes extending from the centre of the galaxy. Another common characteristic of these objects has proved to have high luminosity in X-rays (Elvis *et al.* 1978).

Blazars

Low-frequency catalogues revealed another type of radio-loud objects, that had unusually flat radio spectra.

Object known as BL-Lac became a classical representative of this kind of spectra (MacLeod & Andrew 1968). This highly variable radio source was visible also in optical wavelengths, however, the spectrum had a non-thermal origin and did not exhibit any spectral features (Stein 1978). High-quality long-exposure spectra had to be taken to find at least a few weak emission lines to put constraints on the distances. These observations revealed that objects of BL-Lac category are relatively low-redshifted with $z < 0.2$ (Longair & Malcolm S. Longair 2011).

Similiar highly-variable radio and optical sources that resembled BL-Lac category were found to be 'Optically Violent Variable objects' or OVV. They too possess similar properties as BL-Lac, however, strong broad emission lines were also present in the quasars. Redshifts, at which they are observed, are higher than in the previous case $0.1 < z < 2$ (Longair & Malcolm S. Longair 2011). Nowadays, the name FSRQ (Flat-Spectrum Radio Quasar) is more commonly used for the type OVV quasar.

Both BL-Lac and FSRQ subgroups were later assigned to be part of the same group of Active Galaxies named Blazars. Their common characteristics, apart from high-variability, are high degrees of linear polarisation and observed phenomenon of the superluminal motions (due to projection effects apparent speed in jets exceeds the speed of light).

Unification of Radio galaxies

Similarly to the Seyfert galaxy unification, radio-loud galaxies can be unified under one structure on the basis of the projection effects as shown in the upper part of figure 1.1.

When the inclination is bellow 10 degrees, we observe blazar type of objects. The relativistic jet producing radio lobes is aligned almost directly along our line of sight and flat radio spectra are produced. For higher inclinations we see radio-loud quasars. Similarly to Seyfert classification, quasars can be also distinguished between type 1 (BLR) and type 2 (NRL) depending on the angle and observed narrow and broad features.
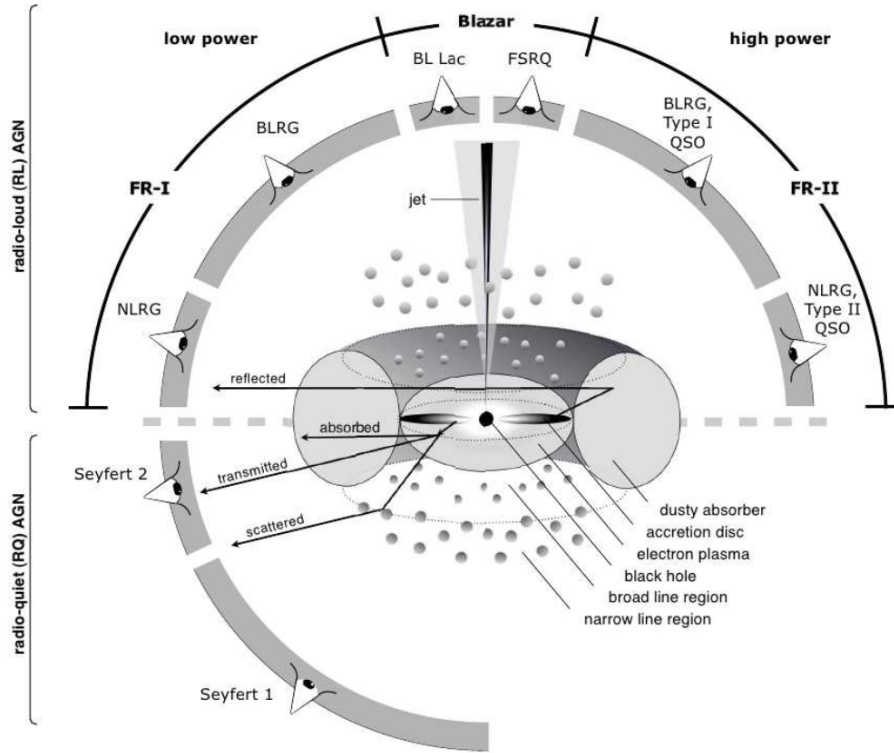
Figure 1.1: Unification scheme of active galaxies as understood today (Beckmann & Shrader 2012). On the bottom of the figure are classes of the radio-quiet AGNs according to the projection angle while on top are classes of radio-loud AGNs. Top of the figure is further divided by the luminosity of AGN, but for simplicity of our text, we do not distinguish between them.

1.2 Geometrical structure of the nucleus

In the previous section, we introduced a classification of the AGNs with division into radio-quiet and radio-loud classes. Geometrically speaking main difference between them is the presence of relativistic jets and lobes causing radio emission. NGC 985 analysed in the later chapter is considered to be radio-quiet Seyfert 1 galaxy, therefore, we focus on the geometrical structure of this group.

1.2.1 Innermost regions

Black holes

The core of every active galaxy is the supermassive black hole that can be defined as supermassive object creating a volume of space-time with the gravitational field so intense that no electromagnetic radiation can escape from it. Famous 'No-hair' theorem said by american theoretical physicist John Wheeler describes black holes as objects, that are distinguishable to the observer only by three quantities - the mass (M), the angular momentum (J) and the electrical charge (Q) (Misner, Thorne & Wheeler 1973). For the case of both the electrical charge and momentum beeing zero, we get Schwarzschild black hole.

The solutions of general relativity equations for Schwarzschild metric yield two important radii. The first one is the Schwarzschild radius (or event horizon) from bellow which, no particle, photon or information can escape and is defined as

$$R_s = \frac{2GM}{c^2} = 2r_g,\tag{1.1}$$

where G is gravitational constant, M the mass of the black hole and c is the speed of light. For simplicity, the term $\frac{GM}{c^2}$ is sometimes also referred to as the gravitational radius r_g.

The second important radius is the marginal stable circular orbit (also known as ISCO)

$$R_{ms} = \frac{6GM}{c^2} = 6r_g.\tag{1.2}$$

Outside of R_{ms} test particles can travel around black hole in circular orbits. However, after the test particle reaches R_{ms}, it's orbit becomes unstable and starts to spiral into the center of gravity.

For rotating black holes (called Kerr black holes) dimensionless spin parameter a can be introduced

$$a = \frac{cJ}{GM^2}.\tag{1.3}$$

It reaches the value in the range of 0 to 1. The rotation of the black hole can have significant effects on its surroundings because of the R_{ms} dependence on the spin. If the spin is larger than zero, the marginally stable orbit moves closer to the black hole and therefore the flow of matter from the accretion disc can be higher and more efficient.

Accretion disc

The most stable configuration in which particles of matter with angular momentum fall onto the central object with mass is the accretion disc. The particles get rid of their

redundant angular momentum through the viscous forces and descend to the further lower orbits. Most of the matter will move this way into the central parts of the disc while a smaller portion will go in the opposite direction and extend the disc (Lynden-Bell & Pringle 1974; Pringle 1981).

Infalling matter also has to dispose of the gravitational potential energy it gathered by approaching the centrum of gravity and it does it locally through the process of viscous dissipation. This creates composite blackbody spectrum with the peak, in a case of AGNs, at around $\sim 10^5$ K lying in the UV (Netzer 2006). Dissipation of energy guarantees cooling of the accretion disc that can be much thinner compared to the disc radius. The so-called 'thin disc' was introduced by Shakura & Sunyaev (1973). Model of the disc was later updated for general relativity corrections by Novikov & Thorne (1973). These geometrically thin, but also optically thick accretion discs are formed and maintained for a large range of AGN luminosities $10^{-4} \leq L/L_{\mathrm{edd}} \leq 0.3$ (Netzer 2006). L_{edd} is the Eddington luminosity, the maximum luminosity of the source when radiative force outwards and gravitational force inwards are equal.

Corona

Even though accretion discs can reach relatively high temperatures, they could not sufficiently explain the amount of radiation observed in X-rays. Therefore, there must be another hot medium in the vicinity of the accretion disc, where more energetic photons could be emitted (Liu & Mineshige 2002; Liu, Mineshige & Ohsuga 2003; Mushotzky, Done & Pounds 1993). This hot medium is nowadays known as the corona.

The process of formation of the corona with temperatures as high as 10^9 K is not fully understood even today, however, magnetic field reconnection is considered to be a relevant process (Wang & Cen 2016). Therefore, the position of the corona is assumed to be just above the accretion disc.

This disc-corona configuration can reasonably account for the observed X-ray radiation. UV photons that emerge in the accretion disc are Compton up-scattered by the hot thermal electrons in the corona. Such physical process leads to a power-law spectrum. In addition, the primary X-ray radiation that is created this way, illuminates the accretion disc again, thus creating the reflection spectra. Reflection components in X-ray are indeed observed, with iron Kα line present in many sources (Fabian *et al.* 1989; Reynolds & Nowak 2003; Tanaka *et al.* 1995).

1.2.2   Broad and Narrow line region

After the X-ray photon is emitted in the central parts of the AGN, it continues on its way out of the nucleus. However, before leaving the nucleus of the galaxy, such photon

travels through several regions where it could be absorbed. Both properties of the matter and the environment change depending on the distance. The closest one to the source is the Broad Line Region (BLR) while in the more distant parts it comes across the Narrow Line Region (NLR).

Broad Line Region

BLR is the region of space above the accretion disc where gas clouds with large column densities ($\sim 10^{23}$ cm^{-2}), high densities ($\sim 10^{10}$ cm^{-3}) and velocities of the order of several thousand km s^{-1}. Moreover the ionising flux is assumed to reach $L/4\pi r^2 \simeq 10^9$ erg s^{-1} cm^{-2} (Netzer 2006). The reverberation[1] studies (Kaspi *et al.* 2005; Peterson 1993) suggests the distance to be bellow 1 parsec from the source.

Clouds in this region are also known to cause eclipsing events of the timescales from hours to days observed in several sources like NGC 1365 (Risaliti *et al.* 2005, 2007, 2009), NGC 6388 (Elvis *et al.* 2004) or NGC 3451 (Puccetti *et al.* 2007). Such eclipses can provide further information on the geometrical and physical structure of the cloud. For example in the case of NGC 1365 analysis of two subsequent eclipses revealed a 'cometary' shape of the cloud with high-density head and elongated lower density tail (Maiolino *et al.* 2010).

Narrow line region

Compared to the broad line region, NLR can also be viewed in the Seyfert 2 galaxies, where torus is obscuring the central source. Lower column densities ($\sim 10^{20-21}$ cm^{-2}), densities of the clouds ($\sim 10^4$ cm^{-3}) and velocities reaching only hundreds of km s^{-1} are observed. Ionising flux associated with the NLR also reaches lower values due to the distance from the source, $L/4\pi r^2 \simeq 10^2$ erg s^{-1} cm^{-2} (Netzer 2006). As the result of the lower density and flux, more forbidden emission lines emerge in the spectra.

Studies of the nearby Seyfert galaxies have shown that NLR can be spatially resolved and that it occupies a cone-shaped region of space spanning from several tens to hundreds of parsecs (Bergmann 2014). This cone-shaped form is produced by the dusty torus that collimates ionising flux over and bellow the accretion disc. In the near future, interferometric observatories like ALMA will give us even better spatial resolution, hence better view into the circumnuclear regions of AGNs (Pérez Beaupuits, Wada & Spaans 2011).

---

[1]Reverberation mapping is a powerful tool to study the innermost parts of the AGNs. It was developed by Blandford & McKee (1982) and is used today for determining geometry and kinematics of BLR together with the mass estimation. It works on the principle of observed variations in the continuum flux and time delay from the reflection of the more distant clouds.

Warm absorbers

Between the BLR and NLR, at distances of 0.1–10 pc from the centre (Netzer 2013), X-ray spectra showed signs of absorption by high ionised gas. This gas is known by name Warm Absorber (WA) and was first evoked to explain absorption in the Einstein observatory data of the quasar QSO MR2251-178 (Halpern 1984). Since then, WAs were observed in about 50 % of nearby Seyfert 1 galaxies (Blustin *et al.* 2005).

The strongest absorption lines in the X-ray spectra are produced by H-like and He-like ions of O, Ne, Mg, Si, S, and Ar as well as Fe XVII-Fe XXI L-shell lines (Reeves *et al.* 2004). Fitted column densities span in the range of $10^{21\pm1}$ cm^{-2} (Netzer 2013) and the absorbers are usually seen in an outflow from several hundred to several thousands of km s^{-1} (Blustin *et al.* 2005). Ionisation plays important role in the shape of the absorption and therefore WAs are described by ionisation parameter defined as

$$\frac{L_{1-1000 \text{ Ryd}}}{nR^2} \tag{1.4}$$

where L is the ionising luminosity in the 1–1000 Ryd, R is the distance from ionising source and n is hydrogen density.

The analysis of a greater number of Seyfert 1 galaxies showed that at the sources where clear signs of WA are registered, spectra could be fitted in average by warm absorber with two distinct ionisation levels. However, many of the higher-quality data showed the presence of third more ionised component. This fact might implicate that number of distinct observed ionisation levels depends on the quality of the data (Blustin *et al.* 2005).

In a number of cases, components appear to be in pressure balance with each other (Krongold *et al.* 2003, 2005, 2007; Netzer *et al.* 2003). This is investigated through the so-called 'Stability Curve' that is discussed in more detail in Section 1.4. Alternatively, it has also been suggested that we could be looking at a single radially-stratified ionisation structure in total pressure equilibrium (Różańska *et al.* 2006).

The origin of the WAs is also a highly discussed topic. The most promising explanations are outflows generated by accretion disc winds (Czerny & Hryniewicz 2011; Elvis 2000; Murray *et al.* 1995) and thermal winds produced by evaporation on the inner parts of the torus (Krolik & Kriss 2001). Several studies have set lower limits for their location to be in the parsec-scale (Behar *et al.* 2003; Netzer *et al.* 2003), suggesting the torus origin. However, other studies found WA to be much closer in a sub-parsec region (Kaastra *et al.* 2004; Krongold *et al.* 2007; Pounds *et al.* 2003) supported by accretion disc origin theory. More studies are therefore required to better answer this question.

The span of ionisation levels ξ of 10^{-2} erg cm s^{-1} up to 10^3 erg cm s^{-1} suggests temperatures of the WAs to be in the range 10^4 up to 10^6 K (Blustin *et al.* 2005). These

temperatures suggest that the absorption caused by the same cloud is visible both in X-ray and UV domain. Indeed, UV and X-ray absorbers are frequently observed together with similar outflow velocities suggesting the same point of origin (Crenshaw *et al.* 1999; Mathur, Elvis & Wilkes 1995; Mathur, Wilkes & Elvis 1998). However, their exact connection is still subject of the research.

1.2.3 Torus

Further from the nucleus, in the scales of 1–100 pc, there is located a dusty obscuring torus with column density greater than 10^{24} cm^{-2} (Bianchi, Maiolino & Risaliti 2012). First observations suggesting the existence of such a region were done by (Antonucci & Miller 1985) as part of their unification theory of Seyfert galaxies. They assumed the geometry of torus with high column density to explain why BLR can't be seen at higher inclination angles.

Even though the initial notion worked with a smooth distribution of the matter inside the torus (Pier & Krolik 1992), nowadays more elaborate models made of clumps (Dulle-
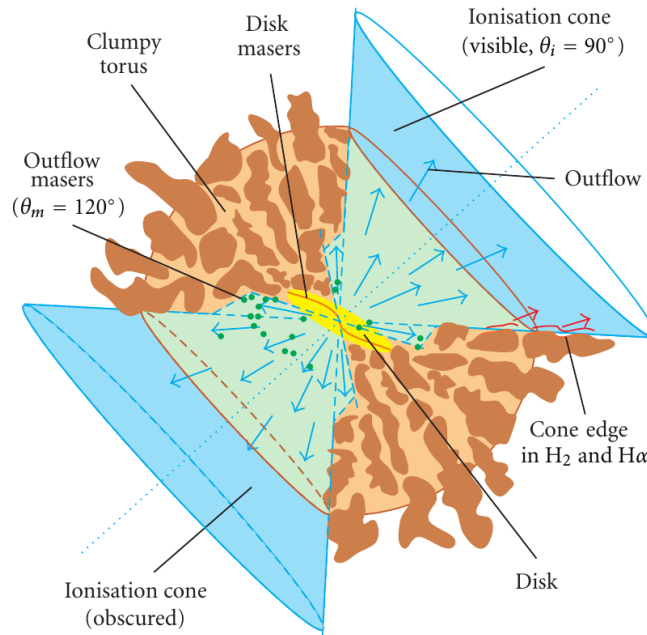

Figure 1.2: The dust torus made of clumps (brown) as derived from the mid-infrared interferometric observations. Matter from the accretion disc (yellow) is seen outflowing (blue and red arrows) inside the ionisation cones collimated by the clumpy torus. (Tristram *et al.* 2007)

mond & van Bemmel 2005) or composite structures of both (Stalevski *et al.* 2012) are considered. All these models are axisymmetric and the torus inner walls are assumed to be at the sublimation radius, where dust evaporates to the gas (Netzer 2015). Inner walls of torus also work as collimators of the radiation and create ionisation cones, where NLR is observed.

The progress in the mid-infrared interferometry allowed mapping of the dust at parsec resolutions. Analysis of the data of Seyfert 2 galaxies NGC 1068 (Jaffe *et al.* 2004; Raban *et al.* 2009), NGC 4151 (Burtscher *et al.* 2009) and Circinus galaxy (Tristram *et al.* 2007) showed two-component dust distribution of distinct temperatures. In the case of Circinus galaxy displayed in figure 1.2 inner warmer component ($T = 330$ K) appears to be 0.4 pc thick while the outer ($T = 300$ K) reaching the thickness of 2 pc (Tristram *et al.* 2007).

1.3   X-ray line diagnostics

Line diagnostic technique is a powerful tool in astrophysics to determine the properties of the environment from where lines originate. It can be used to resolve the main ionisation process in the medium, but also, give constraints on the electron temperature and density (Porquet & Dubau 2000). We use line diagnostics in Chapter 4 for determination of the main ionisation process, therefore, we discuss only this part of the method.

Diagnostics of the leading ionisation process in X-rays is done through He-like ions (atoms with two electrons around the nucleus) such as O VII, Ne IX, Ne IX, N VI and others. Simplified Grotrian diagram of He-like ions can be seen in figure 1.3. There are 3 main radiative transitions depopulating the higher shell levels named resonance (r), intercombination (i) and forbidden (f). Transitions of these lines are listed in the table 1.1. By detecting the strength of each of the lines of a certain element we can infer numerous physical parameters of the matter.

Line	Label	Label in fig. 1.3	Transition		
Resonance	r	w	1s2p ^{1}P$_1$	->	1s^2 ^{1}S$_0$
Intercombination	r	x+y	1s2p ^{3}P$_{1,2}$	->	1s^2 ^{1}S$_0$
Forbidden	f	z	1s2s ^{3}S$_1$	->	1s^2 ^{1}S$_0$

Table 1.1: Most intense lines produced by He-like ions. Figure adopted from (Porquet & Dubau 2000).

If the photoionisation processes are dominant in the medium strongest lines in the spectra observed are forbidden and intercombination lines. In this medium, the intensity of resonance line would be very small compared to the others. On the contrary, if the
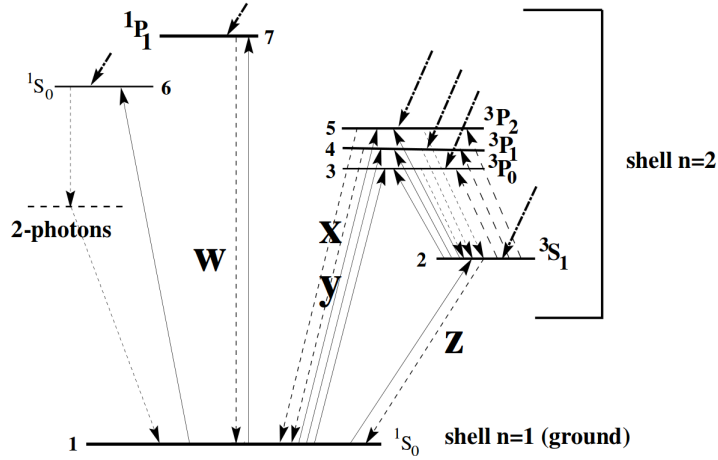
Figure 1.3: Simplified Grotrian diagram of He-like ions. Source: Porquet 2002

intensity of resonance line is comparable or higher than the other lines, it could mean that collisional processes can't be neglected and they may even dominate. Furthermore, if we would know the ratio of ionic abundance of H-like/He-like we could infer the electronic temperature of the diagnosed medium (Porquet & Dubau 2000).

1.4 Systematic stability curve analysis

The effects of various factors on the warm absorber can be studied using the curve of thermal equilibrium. To obtain the curve, energy and charge conservation equations must be calculated. This is done through photoionisation codes such as CLOUDY (Ferland *et al.* 2013) that model the ionisation, chemical and thermal state of material exposed to an external radiation. Results of such calculation can be used, among other applications, to create thermal equilibrium curve, where the heating balances the cooling. The so-called stability curve is given as a function of temperature T on the pressure ionisation parameter Ξ defined as:

$$\Xi = \frac{\xi}{4\pi c k_B T}, \tag{1.5}$$

where ξ is the ionisation defined by equation 1.4, c is the speed of light, k_B the Boltzmann constant and T is temperature.

The positions under and above the curve are unstable and if the gas is located there, it will heat or cool until it reaches the curve. The stability is achieved when photoioni-

sation is balanced by recombination, and ionisation and Compton heating are balanced by recombination and Compton cooling (Chakravorty *et al.* 2012). Time-scales of such events are known to be short, in the case of warm absorbers times shorter than a day were measured (Nicastro *et al.* 1999).

The parts of the curve where the slope is positive $(\mathrm{d}T/\mathrm{d}\Xi > 0)$ are stable against small isobaric perturbations (vertical displacement from the curve). If perturbation happens in the stable region of stability curve, heating or cooling processes will guarantee that it will return back. However, if small perturbation happens in the unstable region, where the slope of the curve is negative $(\mathrm{d}T/\mathrm{d}\Xi < 0)$, the medium starts to cool down away from the original position in the plane.

If two or more warm absorbers with distinct ionisation levels appear on the stability curve within the same values of pressure ionisation parameter Ξ, they are both in the pressure equilibrium. This means they could exist within one physical structure. However, multiphase nature of the warm absorber can exist only under specific conditions. Ionising continuum plays a significant role in the shape of the curve. The best probability for the
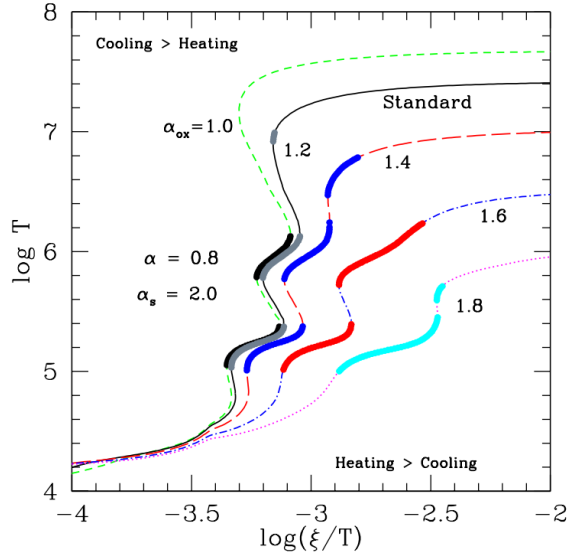

Figure 1.4: Stability curves displayed for different UV to X-ray ionising continuum profiles (given by α_{ox}) and X-ray continuum profile fixed to $\Gamma = 1.8$ ($\alpha = 0.8$ in figure). Stable regions of the stability curve in the temperature range $10^5 - 10^7$ eV are highlighted as bold regions. For example, in the case of the 'Standard' grey curve ($\alpha_{ox} = 1.2$), multiphase nature of the absorber can appear in the pressure equilibrium in three distinct ionisation (and temperature) phases around $\log \xi/T = -3.2$ ($\log \Xi \propto \log \xi/T$). Figure adopted from Chakravorty *et al.* (2012).

stability curve to allow the multiphase nature is when the slope of X-ray ionising continuum is around $\Gamma = 1.8$ (where Γ is photon index of continuum defined as Flux $\sim e^{\Gamma}$). We also show how different profiles affect the shape of the curve in the figure 1.4. Another condition affecting the possibility of the multiphase warm absorber is the metallicity of the gas. The higher it is, the greater probability of finding acceptable stability curves (Chakravorty et al. 2009).

Chapter 2

X-ray disc reflection of the accretion disc

2.1 X-ray disc reflection

Part of the radiation produced by corona, discussed in section 1.2.1, illuminates local structures (accretion disc, BLR clouds, torus) that can be optically thick enough to cause a reflection. One of the most prominent reflection features observed in the X-ray spectra is the Kα iron line. The profile of this line can provide a lot of information about both the properties of the reflecting matter and irradiating source.

In some cases very broad iron lines are observed, which suggests that the radiation may be reflected from the innermost parts of the accretion disc (Fabian *et al.* 1989). By analysing their profile, we can get information about the vicinity of the black hole, such as constraints on the position of the marginally stable orbit and hence the spin of the black hole. Broad red tails of the lines have been detected with clarity in several AGNs such as MCG 6-30-15 (Vaughan & Fabian 2004) and 1H0707-495 (Fabian *et al.* 2009).

Another way to study the innermost parts of the AGN is the reverberation technique (Blandford & McKee 1982). This approach follows the light curves of the primary power-law component and searches for a delay in the light curves of the observed reflection features. Structures as the BLR clouds or different parts of the accretion disc can produce time delays (or time lags) from which the distance between the object and illuminating source can be inferred.

Reflected radiation from the accretion disc can also provide useful information about the properties of the irradiator, the corona. By investigating the reflection profiles of different parts of the disc (defined later as radial-emissivity profile), characteristics such as size and location of the corona can be deduced.

Reflection from various structures in the vicinity of the black hole can say us a lot about the conditions prevailing in the innermost parts of the AGN. It is, therefore, essential to understand how different estimations affect the measured parameters.

2.2   Radial-emissivity

X-ray reflection from the accretion disc can be described by the radial-emissivity profile. It defines how much of the radiation from the primary source is reflected from the disc and irradiated in the direction of the observer. It can be described by a power-law dependence

$$\epsilon(r) \propto r^{-q} \tag{2.1}$$

where q is the radial-emissivity index. This form of the emissivity profile is motivated by the calculations tracing rays in the vicinity of the black hole, from the coronal X-ray sources to the accretion disc (Wilkins & Fabian 2011).

For simplest case when point-like source irradiates thin accretion disc (Shakura & Sunyaev 1973) in flat Euclidean spacetime, emissivity is given by inverse square of the distance from the source multiplied by the incident angle

$$\epsilon(r) \sim (r^2 + h^2)^{-1} \cdot \cos(\theta) \tag{2.2}$$

where r is radius of the disc, h is height of the corona on the rotational axis above the black hole and $\cos(\theta)$ can be expressed as

$$\cos(\theta) = \frac{h}{\sqrt{(r^2 + h^2)}} \tag{2.3}$$

(Reynolds & Begelman 1997). In this setup, the emissivity profile reaches the form of r^{-3} for outer parts of the disc.

However, when effects of general relativity are considered, thus the Kerr-Newman metric, irradiation of the inner parts of accretion disc is highly enhanced compared to the outer. This transfers into higher measured indices for low heights of the corona. Ray-tracing simulations made by (Wilkins & Fabian 2012) confirmed this view and theoretically reached indices of values $q \sim 4$–7 in the innermost parts of the disc.

Steep radial-emissivity indices have been so-far reported in several cases of the AGN sources, such as MGC 6-30-15 (Fabian *et al.* 2002; Miniutti *et al.* 2007), 1H 0707-495 (Wilkins & Fabian 2011) or IRAS 13224-3809 (Ponti *et al.* 2010) but also X-ray binaries Cyg-X1 (Fabian *et al.* 2012), GX 339-4 (Miller 2007). In a few of them, values up to $q = 7$ have been measured.

The most recent method of the radial-emissivity profile reconstruction is based on the measurements of the reflected flux contributions from the each part of the radially segmented disc (Sochora *et al.* 2011; Wilkins & Fabian 2011; Wilkins & Gallo 2015). Used model is composed of several components, each differing only in the parameter of radial range it is applied to. By measuring normalisations N(r) (fluxes) of individual components we get radial profile of the reflected flux, thus the emissivity profile. We applied the method to the real data of Seyfert 1 galaxy 1H 0707-495 with strong and very broad iron Kα line observed by the XMM-Newton observatory. Our model was composed of power-law and

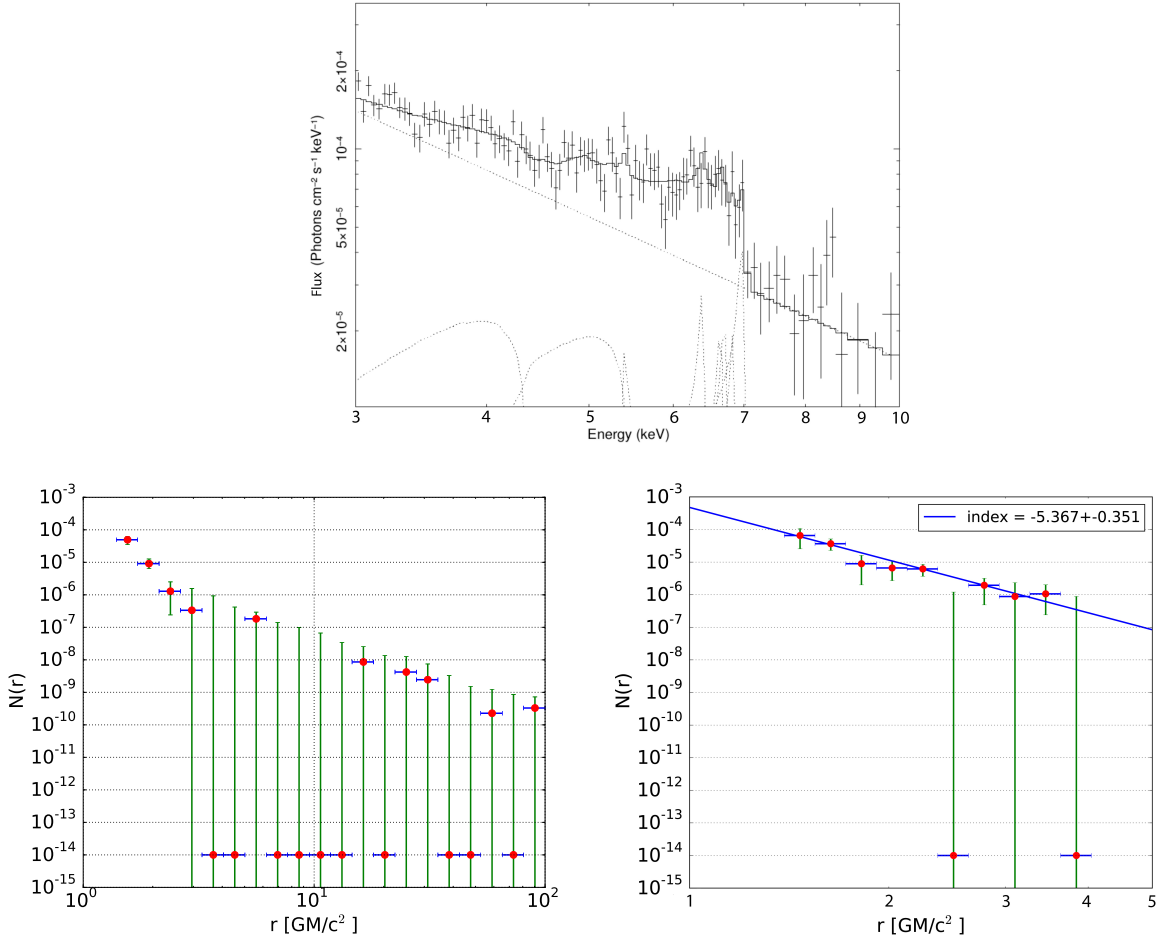**Figure 2.1: Top** Applied radially segmented model on the data of 1H 0707-495. **Bottom** Fitted normalisations N(r) (fluxes) of individual model components on the range of radius **Left** 1-100 r_g **Right** 1-4 r_g. By fitting the slope of normalisations we recieve the radial-emissivity index q.

sum of relativistic iron line models with released normalisation.

$$pow + \sum kyrline(\text{N(r)}) \tag{2.4}$$

We successfully measured the emissivity profile for the innermost part of the disc, however, we could not replicate the results for the larger range. We show our results in figure 2.1.

To visualise how different values of parameter q affect the observed spectrum, we simulate several profiles of the relativistic iron line created by the reflection off the accretion disc. For lower values of q, as shown in figure 2.2 by the blue line, most of the radiation is emitted in the outskirts of the disc and we observe relatively narrow line. However, as radial-emissivity indices steepen, more radiation comes from the inner parts of the disc where the gravitational effects of the black hole are stronger. Photon, that is reflected in this region, therefore, looses part of the energy just to escape from the gravity well. This projects into the shift of the line's maximum to the lower energies. Thus, the higher the emissivity parameter is, the greater shift to lower energies is observed.
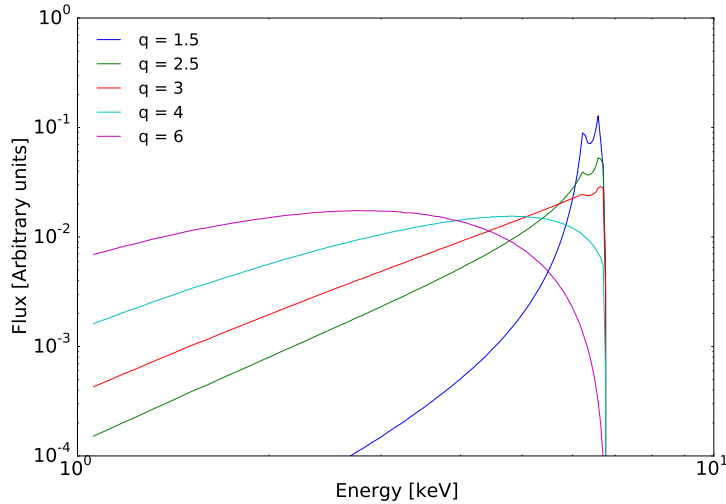

Figure 2.2: Different Fe Kα line profiles modeled with distinct radial-emissivities.

2.3 Lamp-post geometry

The lamp-post geometry is a simplified assumption on how the innermost parts of the AGN generate X-ray radiation. It was introduced by (Matt, Perola & Piro 1991) and (Martocchia & Matt 1996) to explain observed X-ray emission from the accretion disc. The main element of this geometry is a point-like corona (the 'lamp') positioned a few

gravitational radii ($r_g = GM/c^2$) on the rotational axis above the the black hole, see figure 2.3. The height above the black hole directly influences the illumination of the accretion disc, hence changes the observed radial-emissivity profile.

Part of the produced X-ray radiation leaves the system in the direction of the observer (primary power-law component) while the other part could be directed back to the accretion disc. Due to the special conditions prevailing in the vicinity of the black hole, allowing effects such as light bending and aberration to arise, photons fall onto the accretion disc in small angles. Reflection can occur and send photons back to the observer (reflection component).

The recent theoretical work of Wilkins & Gallo (2015) suggests that the corona may, in fact, be small and compact, close to the innermost parts of the accretion disc, therefore, supporting the view of the lamp-post geometry. Another proof of compactness comes from gravitational microlensing of quasars. Recent results from monitoring observations of lensed quasars (Chartas *et al.* 2015) showed that X-ray corona can indeed be as small as 30 r_g. Moreover, microlensing flux variation of the sources like RXJ 1131-1231 suggests continuum producing region to be even smaller than $\sim 10 r_g$ (Dai *et al.* 2009). In the case of NGC 1365 coronal region was suggested to be as small as $\sim 2.5 r_g$ (Risaliti *et al.* 2013).
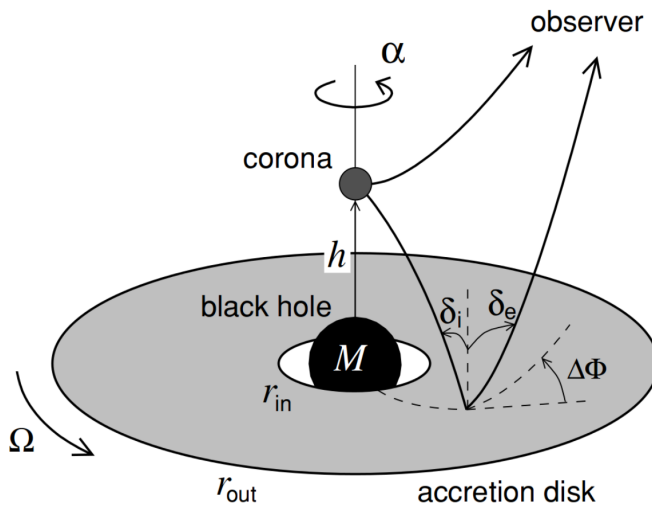

Figure 2.3: The lamp-post geometry scheme. Figure adopted from Dovčiak *et al.* (2011).

2.3.1 Lamp-post approximation and reflection

To demonstrate how reflected spectrum depends on the height of the corona we use again relativistic iron Kα line as an example. We display the line for different heights of primary

corona in figure 2.4.

For greater heights of the corona, more radiation reaches further parts of an accretion disc and then is reflected in the direction of the observer. This interprets into the higher observed flux at the higher energies around the peak of 6.4 keV and is equivalent to the lower values of the radial-emissivity parameter. However, as the height of the corona declines to lower levels, emitted photons reflect themselves off the accretion disc at radii closer to the black hole. Like in the case of the higher emissivity index, photons loose part of their energy to escape the vicinity of the black hole. Lower heights, therefore, cause a greater shift of simulated spectra towards softer X-rays in the same way as high values of q. More research on how these two parameters are connected was done by Dovčiak *et al.* (2014).
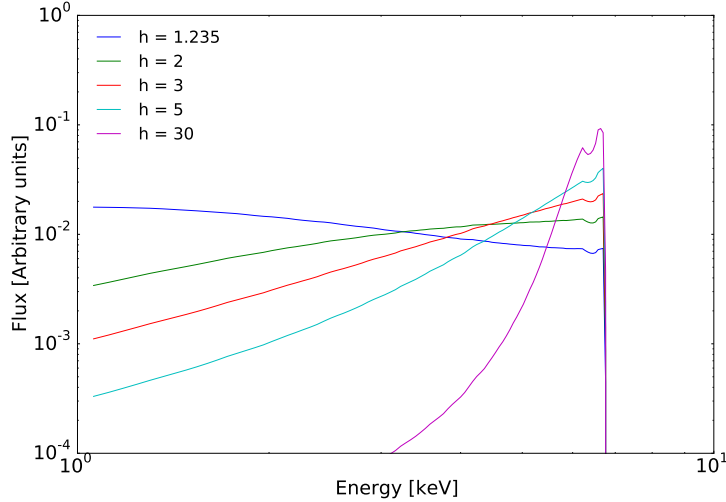

Figure 2.4: Different Fe Kα line profiles in the lamp-post geometry with different heights of corona given in units of gravitational radii.

2.3.2   Ionisation profile

So far we have shown how the height of the corona and radial-emissivity parameter affect spectra of a simple relativistic iron line and how lower heights can cause steeper measured radial-emissivity profiles. Another important parameter of the reflection is the ionisation of accretion disc that is defined the same way as shown in equation 1.4. Different ionisation levels influence the shape of the reflection spectrum, which emission lines are visible and how steep are the spectra. We show this ionisation dependence in figure 2.5.

For the cold least ionised disc number of lines are visible. As the disc gets warmer and

more ionised, the strength of the emission lines declines. In the most ionised case of $\xi = 10\,000$, no lines besides the broad iron line are observed.

Generally, for fitting X-ray spectra, constant ionisation over whole accretion disc is assumed. However, if the central source is compact, parts of accretion disc's surface are illuminated differently causing distinct ionisation levels in each annulus. This kind of radially-stratified ionisation profile can steepen measured radial-emissivity index as shown in Svoboda *et al.* (2012) and therefore constant ionisation may be invalid assumption for reflection spectra of the disc.
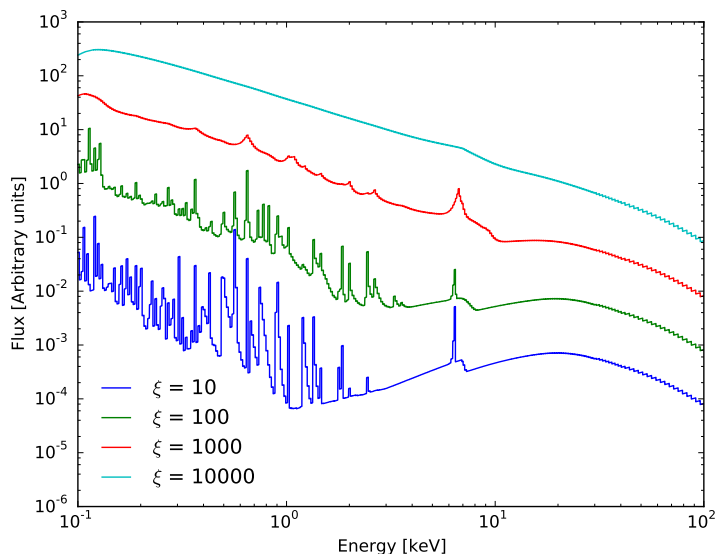

Figure 2.5: Effects of ionisation level on the shape of the spectra. Increasing ionisation of the accretion disc changes the slope from positive to negative in the most important X-ray energies range observed (1–10 keV).

Chapter 3

Systematic study of effects of radially stratified ionisation in the lamp-post geometry

In previous chapter we have discussed how the parameters of height and ionisation affect the shape of the spectra and how they both can steepen the measured radial-emissivity index. The main objective of this chapter is to do a systematic search for conditions, under which the steep radial-emissivity indices q could be reached. We especially consider combining the effects of the lamp-post geometry models and radially-stratified ionisation profile effects on the fitted radial-emissivity parameter.

For our analysis we use a combination of the software tools for X-ray spectral analysis XSPEC version 12.8.2k (Arnaud 1996) and PYTHON version 2.7.6 as XSPEC's wrapper and plotting device. Throughout our study we use reflection model *Reflionx*, several relativistic models of KY code (Dovčiak *et al.* 2004), which include the lamp-post geometry *Kyreflionx* and the relativistic smearing convolution code *Kyconv* (Dovčiak *et al.* 2014) and compare them with other alternative convolution codes such as *Relconv* (Dauser *et al.* 2010, 2013) and *Kdblur* that is based on the calculations of Laor (1991).

3.1   Generating the data

To simulate the spectral data we use XSPEC's *fakeit* command. This tool requires a few parameters such as source model, response matrix of a detector and desired exposition time. Since the longest exposure times achievable by the XMM-Newton (due to satellite's orbit) are around 100–130 ks, we decided to use the value of 100 ks. The resulting spectrum is produced in the standard FITS format.

3.1.1 Seed model

Model *Kyreflionx* from the KY package incorporates both the lamp-post geometry and the radially stratified ionisation and therefore is used for our data simulations. It connects together other models, namely the power-law continuum as the source illuminating corona *Pow*, the accretion disc reflection model *Reflionx* and the relativistic smearing convolution model that redshifts spectrum due to high gravitational effects *Kyconv* as described by equation

$$Kyreflionx \sim Pow + \sum[Kyconv(\Delta r_i) + Reflionx(\xi_i)]. \tag{3.1}$$

It generates accretion disc with different ionisation levels in each annulus that responds to the primary X-ray continuum from the on-axis 'lamp' above the black hole. Final spectrum is, therefore, a sum of X-ray continuum from the primary source (optically thin corona) and reflection from radially-stratified ionisation accretion disc. Since we consider our sources to be out of our Galaxy, we also use *Phabs* model to simulate the galactic absorption. Our final source model has the form

$$Phabs \cdot Kyreflionx \tag{3.2}$$

Throughout our analysis, we use values of the active galaxy MCG 6-30-15 (Fabian *et al.* 2002; McHardy *et al.* 2005; Svoboda *et al.* 2009) as our 'standard' model. They are shown in the table 3.1. We investigate how does the radial-emissivity parameter change in response to different heights of the corona and different densities of the accretion disc (different ionisation levels in the disc).

Parameter	Value	Units	Parameter	Value	Units
a	0.94		density	$10^4 - 10^{-2}$	10^{15} cm^{-3}
theta	30	degrees	density profile	0	
rin	1	GM/c^2	abundance	1	Solar
ms	1		zshift	0.0775	
rout	100	GM/c^2	limb	0	
M	0.1	10^8M$_\odot$	tab	2	
height	1.5 - 9.0	GM/c^2	sw	2	
PhoIndex	2		norm	1	erg s^{-1} cm^{-2}
L	-0.1	L$_{edd}$	phabs nH	4×10^{-2}	10^{22} cm^{-2}
Np:Nr	1				

Table 3.1: Seed model *Kyreflionx·Phabs* used for simulation of the data, where values of the source MCG 6-30-15 are assumed. Detailed description of the *Kyreflionx* parameters is given in the appendix of this thesis.

3.1.2 Response matrices

Response matrix of the detector is given by the combination of two different matrices. The first one, that contains the response of the detector to incoming photons is named 'Redistribution Matrix File' and can be recognised by .rmf extension. The second one, 'Auxiliary Response File' describes the efficiency versus energy relation. It combines together effects of the telescope area, filter efficiency and detector quantum efficiency (together called 'effective area') into one file with extension .arf. By combining these two matrices we get final response matrix (.rsp).

To make our analysis more robust, we decided to use three different detectors to generate and analyse the data. The first one is EPIC-PN detector (Strüder *et al.* 2001) onboard current most advanced X-ray observatory XMM-Newton. Effective area of the PN reaches 1000 cm^2 in the energy range 1–2 keV. Latest response matrix from the 3rd epoch constructed for the full-frame mode of the most centred CCD chip was used in this work. The steep emissivity indices mentioned in the section 2.2 were measured by this particular detector.

The next detector was chosen to be the most advanced detector currently planned – X-IFU (Ravera *et al.* 2014). It should be part of the next-generation X-ray observatory named Athena. This instrument is based on microcalorimeter technology and therefore could be capable of a much better signal to noise ratio. Together with the significantly larger effective area ($\sim 10\,000$ cm^2 at 1–2 keV) it gives better means to investigate reflection spectra. However, since the detector is still in development, with its expected data of launch in 2028, some details could still change. Considering, that we work with relativistic blurred models of the spectra, the resolution of the detector does not play a significant role in our case. For computational speed purposes, we binned the response matrix of X-IFU by a factor of 6 resulting in 4979 energy bins.

As the third one, we chose NICER detector (Gendreau, Arzoumanian & Okajima 2012). This detector has an effective area exceeding XMM-Newton's Epic PN by a factor of two and should be operational on the International Space Station in the early 2017.

We list all of the matrices used in our analysis in the table 3.2 together with release dates and number of energy bins.

Spacecraft	Detector	Date of release	Type	Energy range	No. of bins
XMM-Newton	EPIC-PN	24-11-2014	rmf + arf	0.15-15 keV	4096
Athena	X-IFU	01-04-2016	rsp	0.2-12 keV	29874 → 4979
ISS	NICER	05-09-2013	rmf + arf	0.2-12 keV	1191

Table 3.2: Response and auxiliary files of the detectors used to generate the data.

3.2 Analysis of the data

3.2.1 Analysis model

In this analysis part, we use a combination of models similar to *Kyreflionx* described by equation 3.1 in the data generation part. However, there are two major differences in the analysis model.

First of all, while *Kyreflionx* works with the height of the corona, we want to investigate how does radial-emissivity profile change. Therefore slightly different convolution model *Kyconv* is used in this section. Rather than the height of the corona, broken power-law radial-emissivity with break radius parameters are introduced. Details of used version of the *Kyconv* model can be found in the appendix of this work.

The other commonly used alternatives are *Relconv* and *Kdblur2*. The main difference between them is in the technical design of the code. While *Kyconv* and *Relconv* are more advanced, *Kdblur* is most often used in the analysis as it is one of the pre-installed models in the XSPEC. In our systematic analysis, we use all three convolution models and compare results from them.

Secondly, instead of using radially-stratified ionisation profile of an accretion disc $(\sum[Kyconv(\Delta r_i) + Reflionx(\xi_i)])$ we consider ionisation constant over the whole disc. Hence, we use only one *Reflionx* model rather than the sum of them. This approximation is generally used in accretion disc models and it is our goal to investigate how does simplification like this affect measured radial-emissivity indices.

After inclusion of power-law X-ray continuum and galactic absorption, our analysis model gets the form

$$(Kyconv/Relconv/Kdblur2 \cdot Reflionx + Pow) \cdot Phabs \qquad (3.3)$$

The values of individual parameters are shown in the table 3.3.

Kyconv/Relconv†/Kdblur2*		Reflionx		Power-law, Phabs	
Parameter	Value	Parameter	Value	Parameter	Value
a†	0.94	Fe/Solar	1	PhoIndex	2
theta†*	30	Gamma	= PhoIndex	**norm**	**10⁻²**
rin†*	1	**xi**	**200**	nH	$4 \cdot 10^{20}$
ms	1	z	= zshift		
rout†*	100	**norm**	**10⁻⁵**		
qout†*	3				
qin†*	**7**				
rb†*	6				
zshift	0.0775				
limb†	0				
dE	0.03				
normtype	0				

Table 3.3: Models (*Kyconv/Relconv/Kdblur2·Reflionx+Pow*)·*Phabs* are used for the spectrum analysis. Markers are used to distinguish between the parameters of convolution models *Kyconv/Relconv†/Kdblur2**. *Kyconv* contains all listed parameters. Parameters of models *Kyconv* and *Reflionx* are described in detail in the appendix of this thesis. **Bold** parameters are the free parameters of the fit with initial values. Units of the individual parameters are used the same as in the seed model table 3.1.

3.2.2   Process of handling data and the fitting

Before loading any data for the analysis into XSPEC software we execute grouping of the spectral bins so that every energy bin contains at least 30 counts/detections. This way we ensure that chi-squared statistics can be employed without any problems. After loading the grouped spectra we limit our analysis to the energy range 1–10 keV. Even though we have access to the full energy range of 0.2–12 keV, we decided to not use it due to low count rate over 10 keV and high effects of galactic absorption bellow 1 keV. For correct calculations with *Reflionx* model, a command to extend response matrices up to 100 keV is required.

Our model has 4 free parameters that are left to vary during the fitting. The first two are radial-emissivity and ionisation parameters that we want to investigate. Latter two are normalisations of the primary and the reflection component of the model. These parameters are marked bold in the table 3.3 together with their initial fit guess values.

For all free parameters, errors with 90% confidence levels are calculated. We used Python graphical library to visualise our results, shown in the next section.

3.3 Results

3.3.1 Effects of the compact corona and radially-stratified ionisation on the radial emissivity measurements

In order to investigate the effects of the lamp-post geometry and the radially stratified ionisation profile on the radial-emissivity parameter, we construct several graphs for different disc densities ranging between 10^{14} and 10^{19} particles/cm^{-3} (see figures 3.1–3.3). The x-axis contains heights of the corona for which the simulations were done, ranging between 1.5 and 9 r_g. On the y-axis are displayed fitted values of the radial-emissivity parameter, the ionisation level and the reduced χ^2, defined as χ^2 divided by the degrees of freedom of the fit. All simulations were done with 3 detectors shown in the plots by different colours. We also display ionisation of the accretion disc at 2.2 and 6.0 r_g radius of the seed model. This way we can compare the ionisation levels from the inner parts of the disc with the fitted average value of the whole range 1–100 r_g.

First, we examine effects of the heights of the corona with the *Kyconv* version of the analysis model. In the case of the highest density disc (10^{19} particles/cm^{-3}), the ionisation is low. In this 'cold' disc, a decrease of the radial-emissivity index with the height is evident from the plot. This is due to the light-bending effect that, for low heights, causes a proportionally larger illumination of the innermost region with respect to the outer parts.

As we decrease the density of the disc throughout simulations, the same illumination causes higher levels of the ionisation. We can study effects of different ionisation profiles by comparing results between the densities graphs in the figure 3.1.

In the graphs with lower densities of the accretion disc, we can see a decreasing tendency in the fitted values too. However, in the lowest heights and mildly ionised radially stratified disc (densities 10^{17}–10^{16} particles/cm^3), the radial-emissivity index reaches even steeper values of $q \sim 6$–7. But when the disc gets even more ionised (densities 10^{15}–10^{14} particles/cm^3), maximum values tend to decrease back to $q \sim 4$–5.

Behaviour like this can be explained by the improper approximation of the constant ionisation over the whole disc. When the disc is cold, ionisation in the innermost parts is the same as in the outer parts. Data of the cold disc, therefore, fulfil the condition of the approximation, the constant ionisation over the whole disc. As the ionisation level increases, reflection spectrum is given by the sum of reflection components from differently ionised radii that radiate very different profiles as shown in figure 2.5. When reflection model with the constant density over the whole disc is applied on these spectra, more ionised inner parts are underestimated in the fit while the outer parts are overestimated. This reflects into the higher fitted values of the radial-emissivity index in the inner parts of the disc, that we measure. However, when the ionisation levels increase, even more, the

outer parts of the disc are also sufficiently ionised. Differences between reflection profiles from each radii (figure 2.5 in range of $\xi = 10^4$–10^3 erg cm^{-2} s^{-1}) are smaller and therefore, compensation in the form of higher emissivity index is also lower.

Even though the simulations from the different detectors cast approximately the same results of the fit in the majority of the cases, slight differences still appear. The most prominent is the increased value of the reduced χ^2. The highest values of the reduced χ^2 were for the X-IFU instrument planned for the Athena observatory. These results imply that the current simplified models will not be able to explain the X-ray spectra of the future satellites and more complex models will be needed.

3.3.2   Comparison of other relativistic models

So far, we have discussed the results gathered while using *Kyconv* relativistic blurring model in our analysis. However, we have also employed alternative models *Relconv* and *Kdblur2* for comparison. We present results in the figures 3.2 and 3.3.

While the general conclusions about the influence of the lamp-post geometry and the radially stratified profile of the ionisation on the radial-emissivity index stay unchanged, details like fitted values of the parameters vary. In both alternative models, we observe a steeper drop in the fitted emissivity index in response to the rising height of the corona and fitted steeper emissivity indices in the lower heights. Sudden 'drops' in the fitted values of parameters are present more often than in the *Kyconv*. The cause of the drops is in more details investigated in the next section. We note that computation times of these models were also much longer. When used on the same data it took *Relconv* approximately 20 times longer and with the *Kdblur2* 10 times longer compared to the *Kyconv* model.
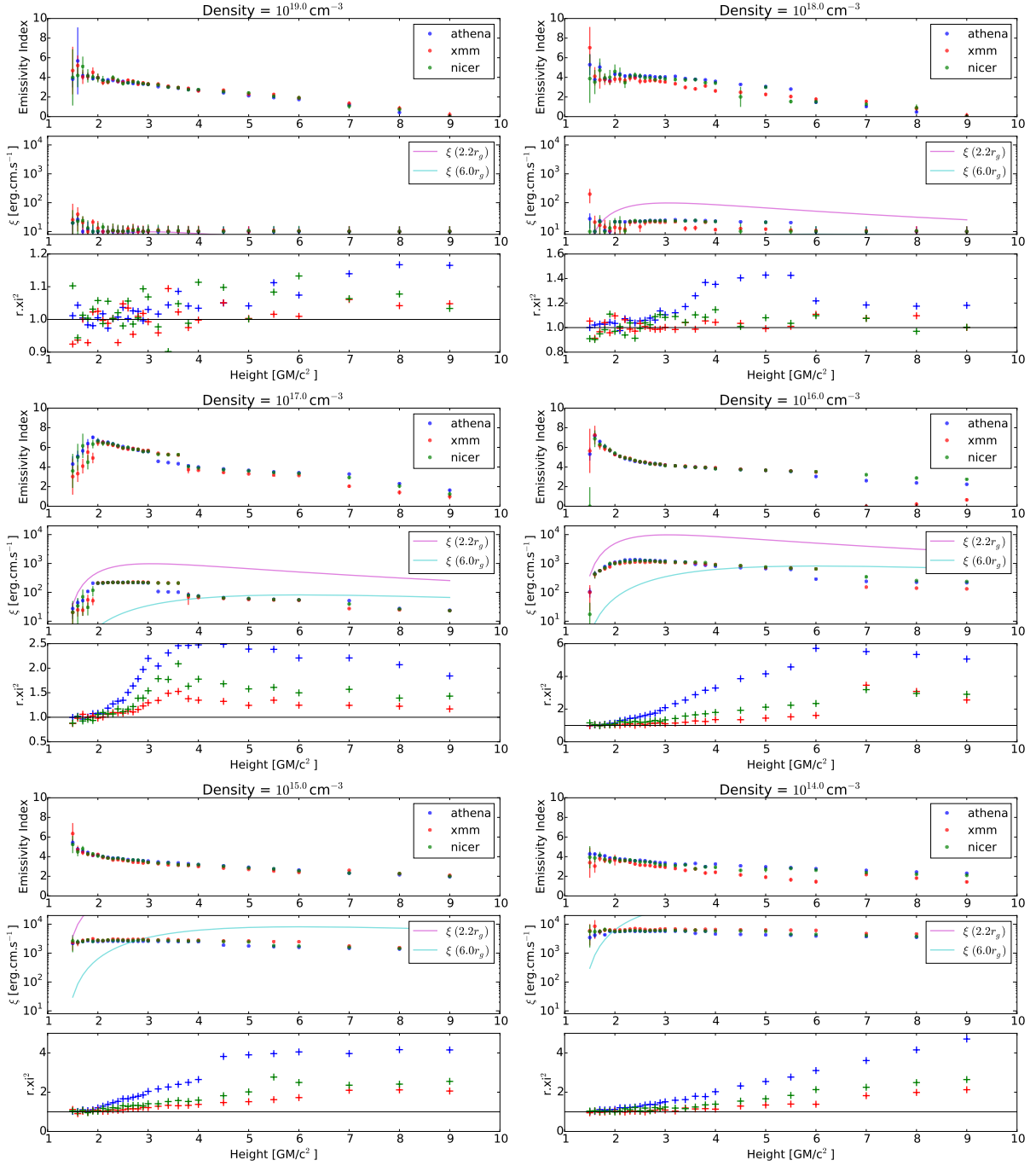
Figure 3.1: Systematic study of the radial-emissivity parameter with *Kyconv* used in the analysis model.
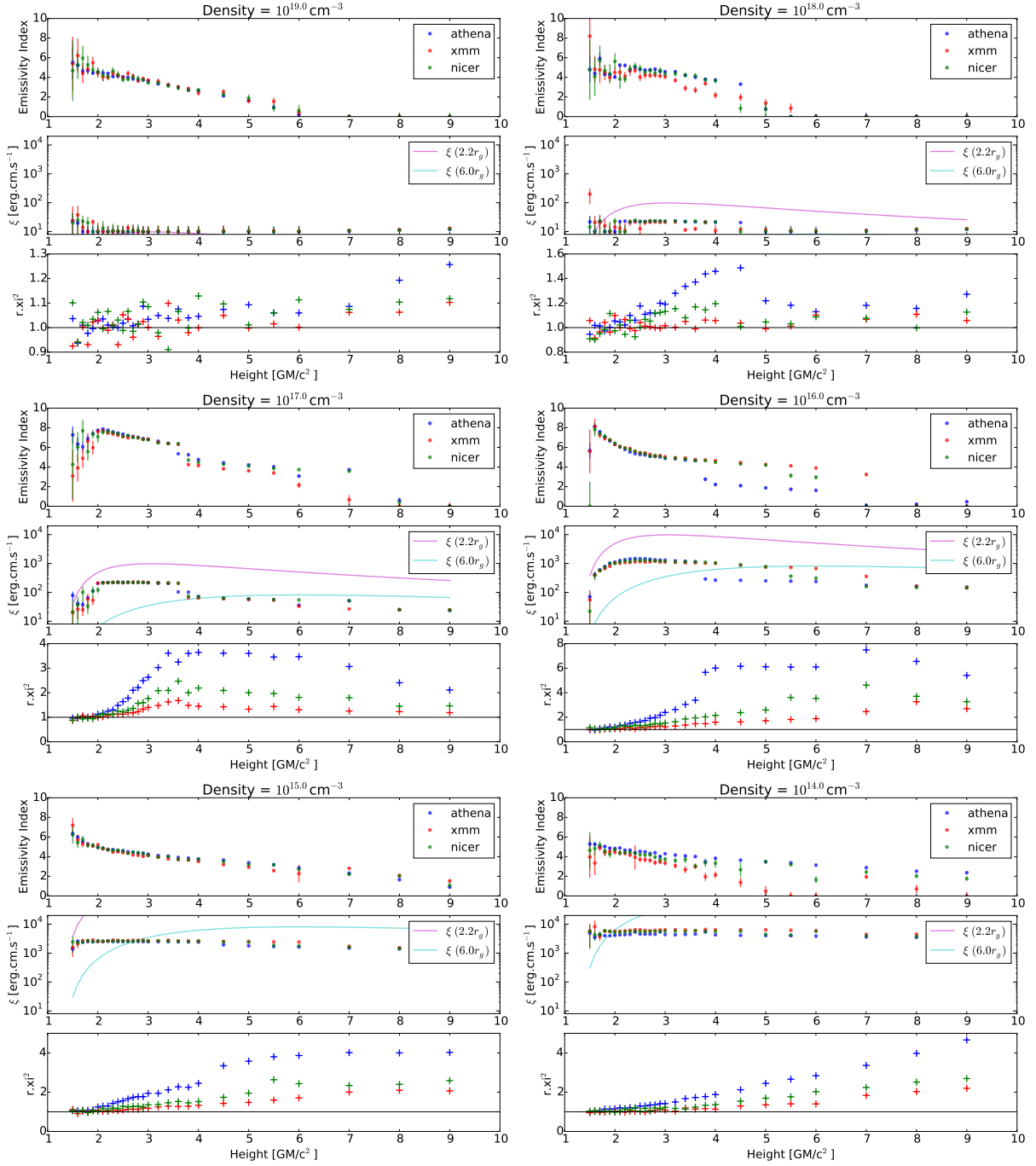
Figure 3.2: Systematic study of the radial-emissivity parameter with *Relconv* used in the analysis model.
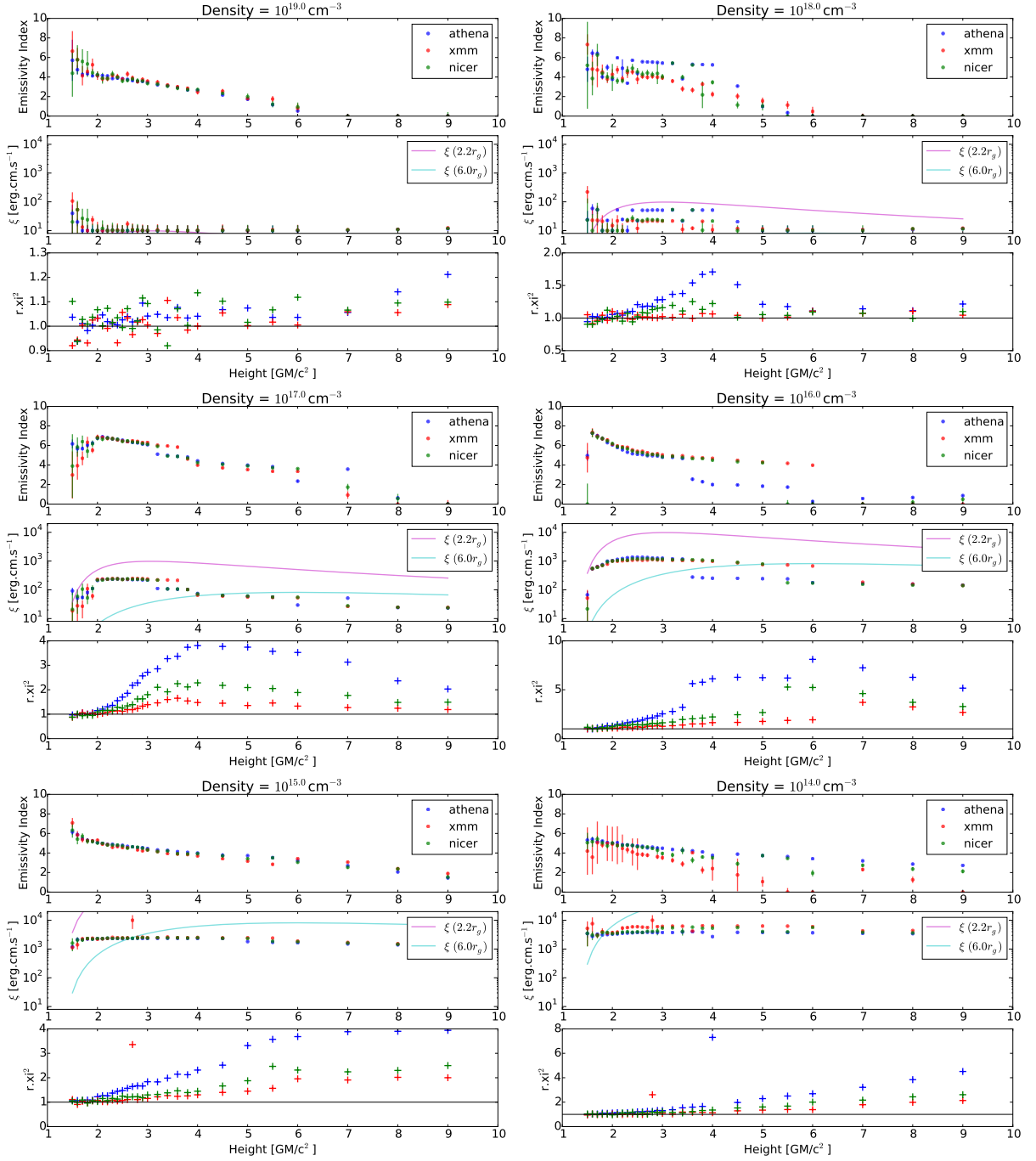
Figure 3.3: Systematic study of the radial-emissivity parameter with *Kdblur2* used in the analysis model.

3.3.3 A closer look at the relation between the ionisation and the radial-emissivity parameter

In order to explain the drops of the fitted values between the heights 3–4 r_g of the graph with disc density 10^{17} cm^{-3} in the figure 3.1, we investigate the fit statistic contour plots of the emissivity index and ionisation. Produced contours for the heights 2.6, 3.0, 3.2 and 3.6 r_g of the X-IFU detector are displayed in the figure 3.4.

These contour plots reveal a large degeneracy between the inner-emissivity index q and the average disc ionisation ξ, implying that the parameter space is complex in despite of that the formal errors corresponding to 90% confidence level of the interested parameters (as shown in figures 3.1–3.3) are relatively small.
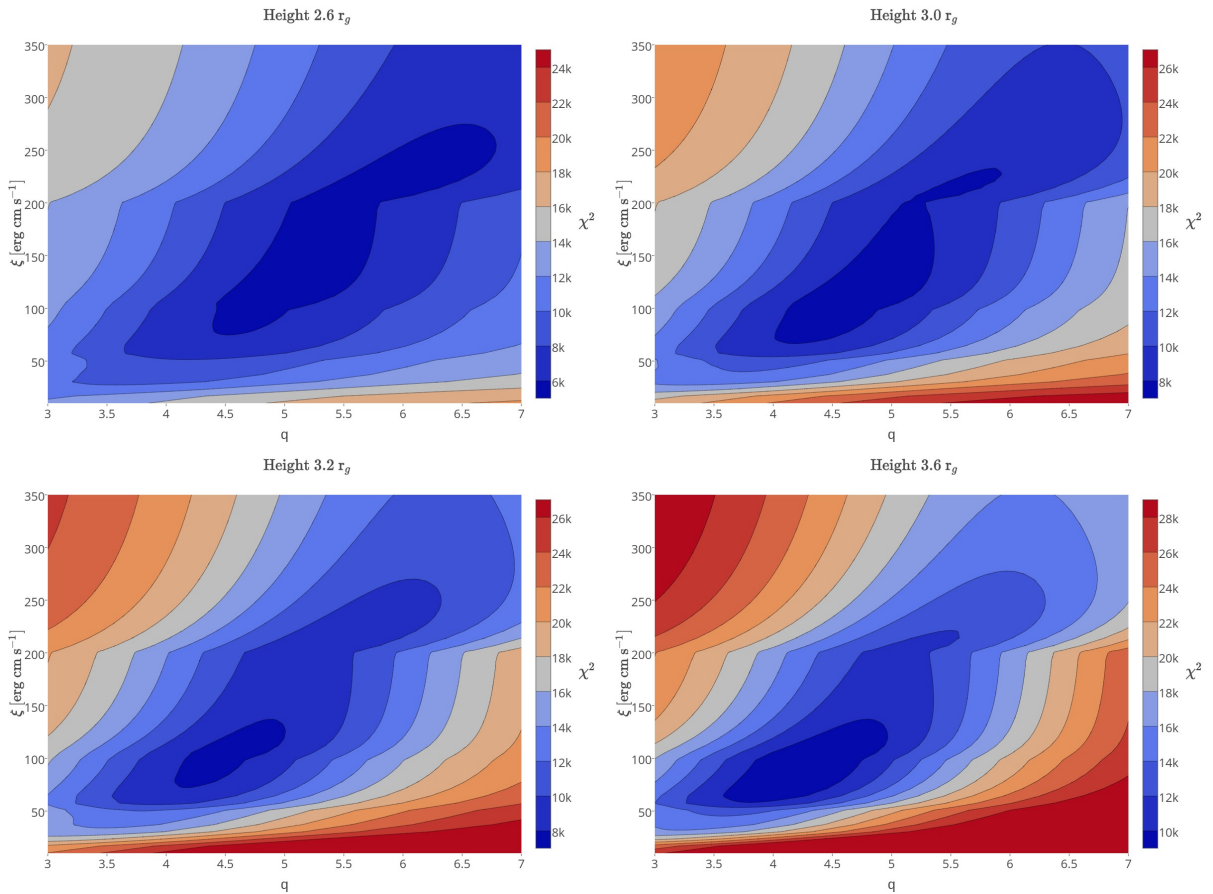

Figure 3.4: Contour maps in the ξ–q plane for the heights of the corona 2.6, 3.0, 3.2, 3.6 r_g and the disc density 10^{17} cm^{-3}.

Chapter 4

Spectral analysis of new X-ray observations of NGC 985

4.1 Historical context

NGC 985 shown in figure 4.1 (also know as Mrk 1048) is a Seyfert 1 galaxy at low redshift $z = 0.0427$ (Arribas *et al.* 1999). With X-ray flux of $F_{(2\text{keV-10 keV})} = 2 \times 10^{-11}$ergs s^{-1}cm^{-2} (Nicastro *et al.* 1998), this active galaxy belongs to one of the brightest ones observed.

It has a distinctive ring-shaped structure that is suggesting an ongoing process of two galaxies merging into one, see 4.1. This was proposed early on in the paper of de Vaucouleurs & de Vaucouleurs (1975). However, the definitive proof of it came after many years as a result of detailed analysis of the optical and infrared observations. Garcia & Espinosa (1996) showed, that there is second spheroidal galaxy interacting with the first one, confirming the status of the galaxy as a merger.

The first detection of NGC 985 in the X-ray waveband was done by the Einstein observatory. Subsequent observation by the ROSAT satellite revealed complex features in its X-ray spectra (Brandt *et al.* 1994). Since data did not provide a good match with the simple power-law model, the presence of the soft excess and ionised absorber was suggested. Later analysis of the ASCA satellite data confirmed the existence of this ionised absorber (Nicastro *et al.* 1999, 1998).

Since then, the source was studied for warm absorber properties multiple times with different observatories. The first observation by Hubble Space Telescope (HST) in UV showed six distinct kinematic components causing the absorption (Arav 2002). At least one of those gas components had sufficient column density to cause absorption also in X-rays. The grating spectrograph HETGS onboard Chandra X-ray observatory actually revealed out-flowing ionised gas in two different ionisation states (Krongold *et al.* 2005). They both

appeared to be in the pressure equilibrium. However, the exposition time of 77 ks was not sufficient enough to say whether these components have also different kinematic properties. In 2003, another observation was conducted, with the XMM-Newton observatory. Analysis of its Reflection Grating Spectrograph (RGS) data confirmed two warm absorbers and even marginally detected third, more ionised component (Krongold *et al.* 2008).

Furthermore, NGC 985 is also showing signs of long-term X-ray variability (Krongold *et al.* 2005, 2008). In 2013, monitoring programme of the Swift satellite discovered an unusual drop of the flux in respect to the past observations of the source lasting several months (Parker *et al.* 2014). This event triggered another immediate joined observation of XMM-Newton and HST. The data revealed that flux bellow 1 keV dropped by a factor of 4-5 while the spectrum above 5 keV stayed essentially unchanged (Parker *et al.* 2014). This behaviour points to the absorption origin of the low-flux state in the AGN and could be attributed to the absorber passing in front of the source.

In the effort to properly analyse ionisation and kinematic structure of warm absorber in this source, another joined set of observations by XMM-Newton and HST was conducted in 2015. The source appeared to get out of the low-flux state back to values from before the 2013's drop. The long-exposure data from the PN detector also revealed complex ionisation structure of the warm absorber showing 4 different components (Ebrero *et al.* 2016). The aim of our work was to simultaneously analyse data from the RGS detector for a better understanding of the warm absorber properties.
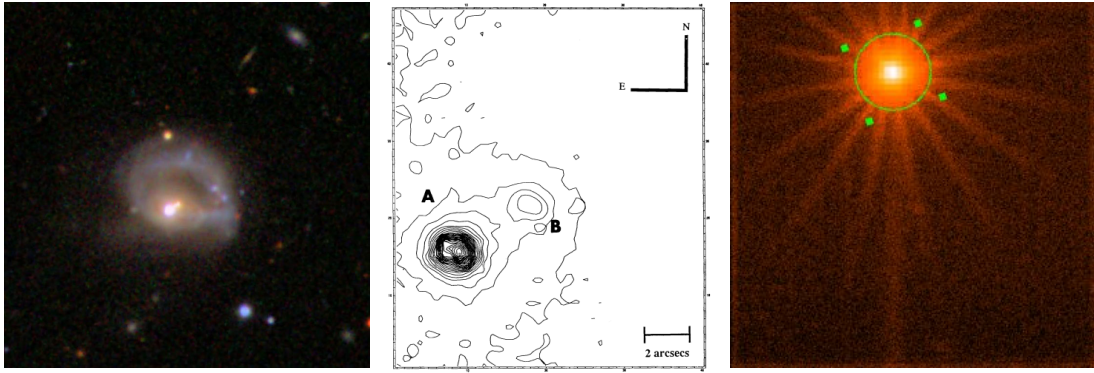

Figure 4.1: Left Ring shape structure of the Seyfert 1 Galaxy NGC 985, SDSS (Ahn *et al.* 2012), **Middle** Near-IR contour map with apparent two nuclei, Protocam, IRTF, K band (Appleton & Marcum 1993), **Right** XMM-Newton EPIC PN detector image from our analysis.

4.2 Data reduction process

Obs. Marker	Obs. ID	Exp. time (ks)	Start date
Obs03	150470601	57.73	2003-07-15
Obs13	690870501	102.16	2013-08-10
Obs15A	743830501	137.22	2015-01-13
Obs15B	743830601	120.38	2015-01-25

Table 4.1: List of observations used in our analysis.

NGC 985 was observed by the XMM-Newton (Jansen *et al.* 2001) 5 times during its ongoing mission, once in 2003 and twice in 2013 and 2015. The details of the observations are given in the table 4.1. One observation of 2013 was excluded from our analysis due to the low exposure time and thereby not sufficient S/N ratio. The main objective of this
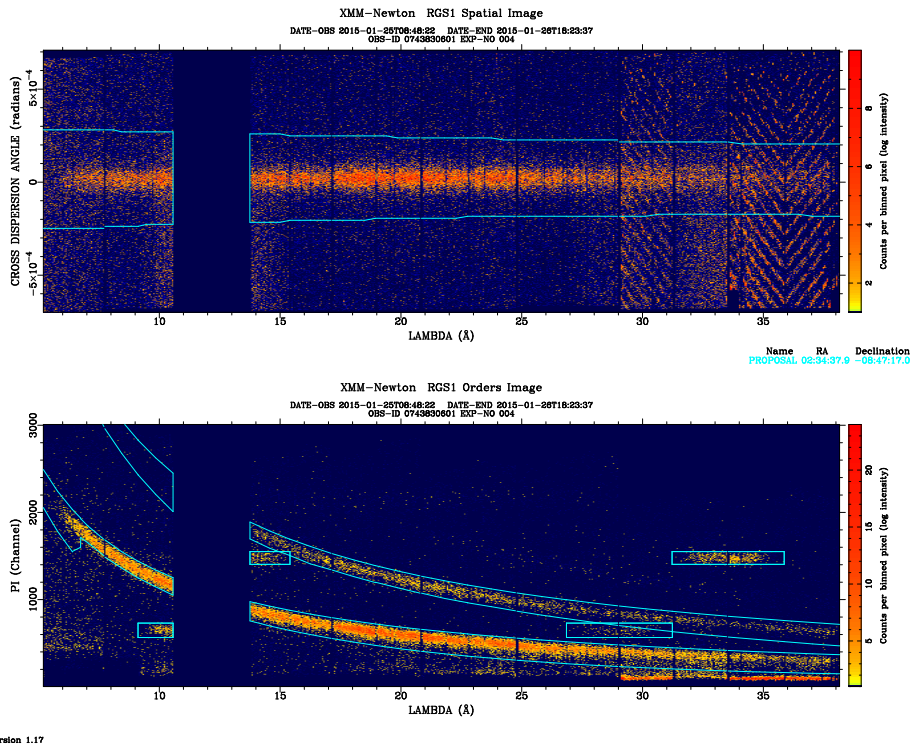

Figure 4.2: Upper Spatial-dispersion angle image of the spectrum on RGS 1 detector. **Lower** Energy-dispersion angle image of the RGS 1 detector. The gap between 10.5–14 Åis caused by a failed CCD chip.

part of the work is the study of data produced by high-resolution RGS detector. These data were taken in the normal spectroscopic mode. We used the XMM-Newton Science Analysis System (SAS) v14.0.0 for all data reduction (Gabriel *et al.* 2004). The *rgsproc* task was used to produce cleaned spectra. After running this pipeline, a check of the correct source selection is recommended. This is done by looking into Spatial-Dispersion angle and Energy-Dispersion angle graph (also known as Banana plot).

If the source is correctly chosen, the mask overlays bins with the strong counts detection. If there was more than one X-ray source in the field of view of the RGS detector, it would show up in these plots as double lines in the masks. In our case we had only one source and no adjustments of the mask was needed. In figures 4.2 and 4.3 we show these graphs for both RGS 1 and RGS 2 detectors. In both detectors gaps in the energy wavelengths appear. These gaps are caused by the failed CCD chips, however, combined data from both detectors still provide spectra in the full range of 6 to 38 Å.
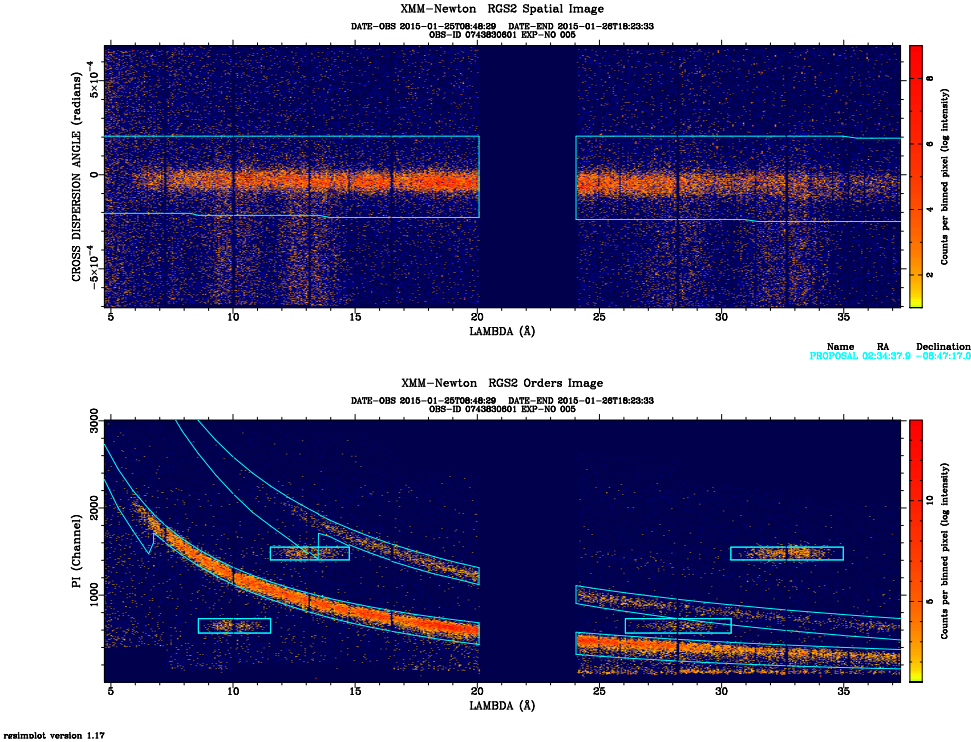

Figure 4.3: Upper Spatial-dispersion angle image of the spectrum on RGS 2 detector. **Lower** Energy-dispersion angle image of the RGS 2 detector. The gap between 20–24 Åis caused by a failed CCD chip.

Another important part of the data reduction is filtering the high particle background that is caused by the Solar activity. It is important to filter these time periods out before any further analysis of the data. In RGS detector high-background is considered when background RATE of counts exceeds value 0.1. As an example, we show this filtering process for observation 2015b data in figures 4.4 and 4.5. Higher values of background radiation on the RGS2 detector are caused by the position of the satellite with respect to the Sun.
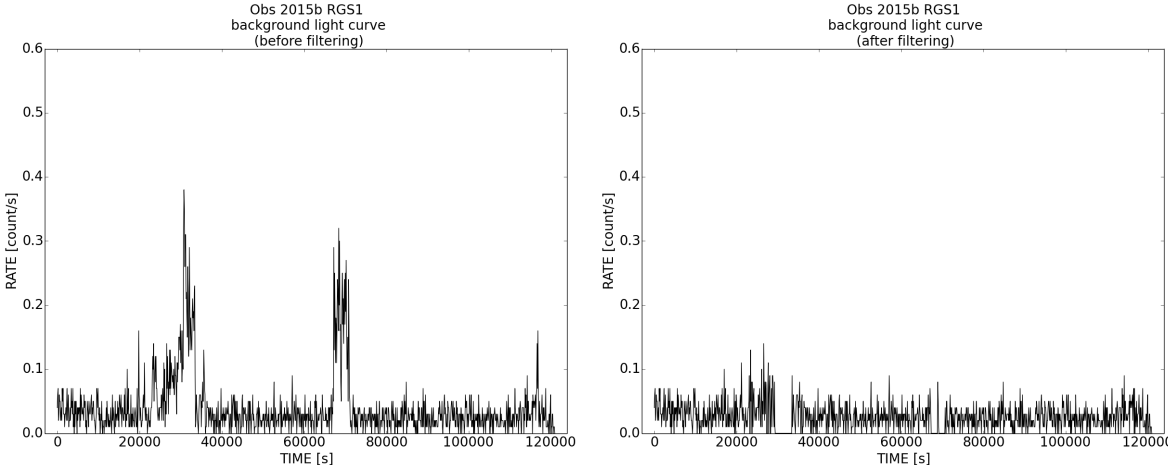

Figure 4.4: Background data of the detector RGS1 **Left** before and **Right** after filtering.
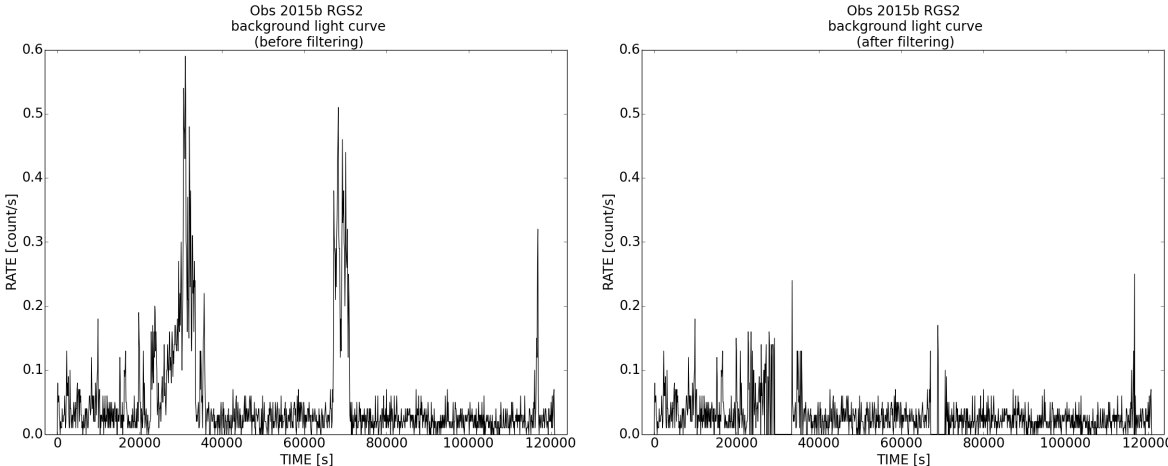

Figure 4.5: Background data of the detector RGS2 **Left** before and **Right** after filtering.

Resulting light curves in figure 4.6 are constructed as the combination of data from both detectors.
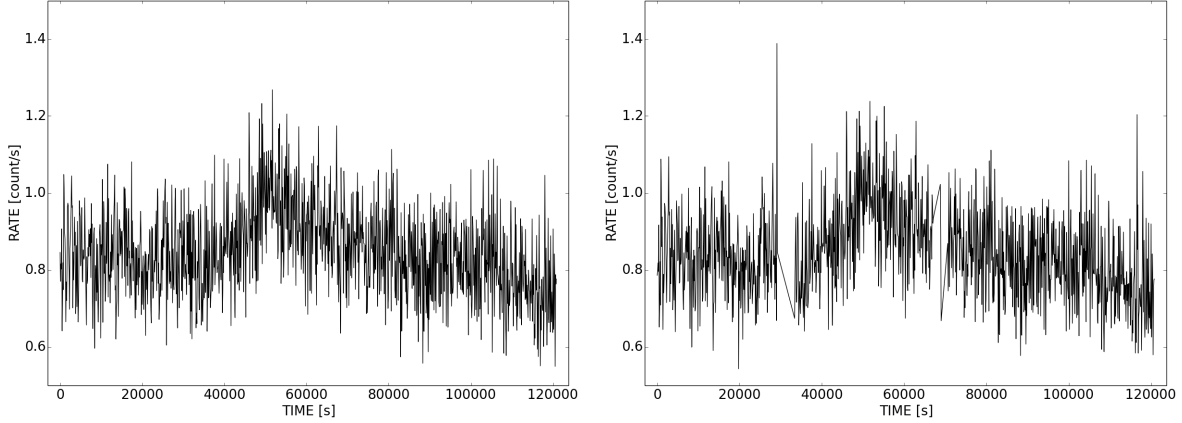

Figure 4.6: Light curve **Left** before and **Right** after filtering.

4.3   SED, CLOUDY and Xabs model

Spectral energy distributions (SEDs) used throughout our analysis were constructed using XMM-Newton's EPIC-pn detector in X-ray and HST's COS detector in the UV. There was no simultaneous HST observation in 2003, therefore, data from the optical monitor (OM) camera onboard the XMM-Newton were used. The X-ray part of the SED was constructed using the best-fit parameters of continuum mentioned in Table 3 of (Ebrero *et al.* 2016). All SED's were corrected for galactic reddening using the formulas provided in Cardelli, Clayton & Mathis (1989). UV data points were also revised for the starlight contamination from the host galaxy by applying the bulge galaxy template (Kinney et al 1996) scaled to the galaxy's flux. For more details about the construction of SED, we refer the reader to section 3 of Ebrero *et al.* (2016).

In our RGS analysis, we also used the second set of SEDs that included absorption by the first UV warm absorber. Resulting SEDs were therefore constructed with the continuum from the first SED affected by absorption properties of the UV absorber. All mentioned SEDs are displayed in the figure 4.7.

Produced SEDs are the basis for the next analysis using the SPEX's model *Xabs*. This model requires input file that contains ionic column densities of the elements together with the electron temperature vs. ionisation parameter dependence. We calculate them with the photoionisation code CLOUDY version 13.01 (Ferland *et al.* 2013) that uses as input the already created SEDs.

The *Xabs* model calculates transmission of the flux through a slab of material. The difference from the simpler model *Slab* is that all ionic column densities are in this model linked through photoionisation balance. We use it to incorporate warm absorbers in our models. One of the main parameters that we are investigating in our analysis is ionisation parameter defined by the equation 1.4. Other free parameters in our model describing warm absorbers are hydrogen column density n_h, root means square velocity inside the gas cloud σ, an average systematic velocity of the absorber v_{out} and covering factor f_c.
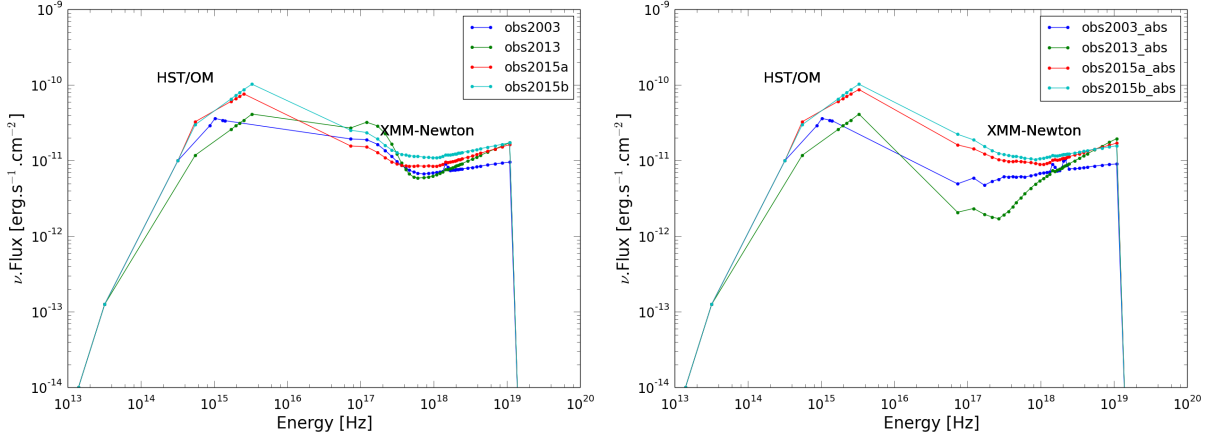
Figure 4.7: Spectral Energy Distribution of NGC 985. **Left** Standard SED adopted from (Ebrero *et al.* 2016). **Right** SED modified by the first absorber.

Constructed SEDs are also used for calculation of the flux and the luminosity of the source for each observation. Since the ionisation parameter definition works with the luminosity in the energy range 1–1000 Ryd (alternatively 13.6–13 600 eV or $\sim3.3\times10^{15-18}$ Hz), we decided to use this range for further calculations. Our computation was done employing trapezoidal method onto the SED and results are provided in the table 4.2. For calculation of the luminosity, values $H_0 = 70$ km s^{-1} Mpc^{-1} and $z = 0.0427$ (Arribas *et al.* 1999) were used.

	Obs2003	Obs2013	Obs2015a	Obs2015b
Flux [ergs s^{-1} cm^{-2}]	9.36×10^{-10}	5.40×10^{-10}	1.17×10^{-9}	1.25×10^{-9}
Luminosity [ergs s^{-1}]	3.75×10^{45}	2.17×10^{45}	4.69×10^{45}	5.02×10^{45}

Table 4.2: Flux and luminosity of the source in the energy range 1–1000 Ryd (13.6 eV– 13.6 keV).

4.4 SPEX analysis and results

Analysis of the spectra was done within the SPEX fitting package (Kaastra, Mewe & Nieuwenhuijzen 1996) version 2.06.01. The fitting method employed was C-statistics (Cash 1979), which is used when the data have the Poisson probability distribution instead of the Gaussian. For the high-quality observations from 2015, the energy range of 7–38 Å was used. We applied the binning factor of 5 for energy range 7–24 Å and factor of 7 for the energy range 24–38 Å. Higher binning was used to compensate for the lower effective area and therefore, higher noise towards the lower energy range. For the observations 2003 and 2013 we were forced to, due to the high background, use data only in the energy range 7–26 Å with chosen binning of factor 7. The reason for that was the low count rate caused by the studied eclipsing event in the case of the observation 2013 and in the observation 2003 combination of the partially covered source and the low exposure time.

4.4.1 Continuum and emission lines

To model the intrinsic continuum of the source we first used simple power-law. Indices of the power-law were adopted from the earlier analysis of the EPIC-PN spectra of this source (Ebrero *et al.* 2016). As a representation of the soft excess was used a modified blackbody model which in addition to the classical blackbody incorporates also coherent Compton scattering, using the formula derived by (Kaastra & Barr 1989). Table 4.3 represents the best-fit values of the continuum parameters for all observations.

Galactic absorption in the direction of the observation caused by the cold gas was accounted through the SPEX's model *hot* with equivalent hydrogen column density set to 3.17×10^{-20} cm^{-2}.

Emission features were modelled by the simple Gaussian models with the centroid wavelengths frozen to the laboratory values. The most prominent line, with the confidence level over 3σ in all analysed observations was the forbidden line O VII (f). Due to the

Model	Parameter	Obs. 2003	Obs. 2013	Obs. 2015a	Obs. 2015b
Power-law	norm	$2.54^{+0.54}_{-0.51} \times 10^{8}$	$9.86^{+2.32}_{-7.27} \times 10^{7}$	$3.86^{+0.61}_{-0.76} \times 10^{7}$	$4.31^{+0.88}_{-0.48} \times 10^{8}$
	Γ	**2.21**	**1.71**	**2.14**	**2.22**
MBB	norm	$3.66^{+7.61}_{-1.62} \times 10^{6}$	$5.13^{+4.10}_{-2.54} \times 10^{7}$	$1.81^{+0.67}_{-0.40} \times 10^{7}$	$3.26^{+0.87}_{-0.55} \times 10^{7}$
	T	$0.18^{+0.05}_{-0.10}$	$0.23^{+0.02}_{-0.01}$	$0.14^{+0.01}_{-0.01}$	$0.116^{+0.008}_{-0.008}$

Table 4.3: Values of parameters in our best-fit continuum model. The parameters of normalisations are in units of flux while the temperature of soft excess is in eV. Γ is a dimensionless parameter of the power-law index. **Bold** values are adopted from previous analysis of EPIC-PN detector Ebrero *et al.* (2016).

lower count rate of the source in the observation 2013, multiple emission lines arose from the continuum. Forbidden line O VII (f) is detected at $\sim 2\sigma$, Ne IX (f) with significance over 4σ and Mg XI (f) at the $\sim 1.5\sigma$. From the intercombination lines only O VII (i) was detected at the 2σ level. In observation 2015a, these lines are visible with the same significance, while in observation 2015b they are not detected. Resonance lines are also present in the observation 2013, namely Mg XI (w) at the $\sim 1.5\sigma$ and also O VII (w) at the $\sim 3\sigma$. The latter was found with the same significance in the observation 2015b. Detection of the prominent forbidden lines and slightly weaker resonance lines suggests that the main ionisation process is photoionisation (Section 1.3). Other lines found were mostly Lα lines of ions such as C VI, N VII, O VIII, Mg XII. All found emission lines

Emission line	Laboratory Wavelength [Å]	Flux [10^{-15} ergs cm^{-2} s^{-1}]	σ
Obs. 2003			
O VII, af	22.0974	30.8 ± 7.5	4.85
Obs. 2013			
Mg XII, Lα	8.421	4.7 ± 3.9	1.16
Mg XI, aω	9.1687	4.5 ± 3.0	1.54
Mg XI, af	9.3136	3.8 ± 2.7	1.48
Ne IX, af	13.6984	6.2 ± 1.6	4.45
O VIII, Lβ	16.0059	2.1 ± 1.2	1.86
O VII, bf	18.7307	3.2 ± 1.6	2.14
O VIII, Lα	18.9689	7.8 ± 1.8	5.22
O VII, aω	21.6015	8.0 ± 2.7	3.44
O VII, ai	21.802	10.8 ± 5.7	2.19
O VII, af	22.0974	21.4 ± 4.1	6.90
N VII, Lα	24.781	3.3 ± 1.6	2.28
Obs. 2015A			
O VII, ai	21.802	10.2 ± 5.4	2.01
O VII, af	22.0974	22.2 ± 5.4	4.52
C VI, Lα	33.735	5.2 ± 2.8	1.90
Obs. 2015B			
O VII, aω	21.6015	12.5 ± 4.7	2.89
O VII, af	22.0974	27.7 ± 7.1	4.35

Table 4.4: List of emission lines detected in our dataset. For each line defined by laboratory value wavelength we calculate flux in the line and significance of detection. L = H–like, a = Heα–like, b = Heβ–like.

are listed with their laboratory wavelengths, significance and occurrence in datasets in the table 4.4.

4.4.2 Warm Absorbers

Absorption features in the RGS spectra are mostly attributed to the partially ionised outflowing gas at the redshift of the source. From the visual examination of the high-quality data measured in 2015, we can already recognise some of the absorption lines. The most prominent ones are caused by elements such as O, N, Ne, Mg and Fe. While few of the absorption lines can be assigned to exact transitions, their identification is problematic due to the blending of multiple neighbouring transitions into a single observed feature.

In our study of warm absorbers, we use SPEX's photoionisation model *xabs*, which calculates the transmission of the photons through a slab of material. All the ionic column densities are linked through a photoionisation balance model calculated by CLOUDY.

We started our analysis with one confirmed UV–X-ray absorber (Ebrero *et al.* 2016) that we added on top of the continuum. Since this lowest ionisation warm absorber had the most prominent effect on the part of the spectrum with the highest background noise and lowest effective area, we decided to adopt values of the parameters ξ, σ and v_{out} from the analysis of the simultaneous HST observation (Ebrero *et al.* 2016). Only parameters left to vary were, therefore, hydrogen column density n_H and covering factor of the source f_c. In the next step, we appended the other *xabs* components with free parameters n_H, ξ, σ and v_{out} until we reached no significant improvement of the fit. We also tested the possibility of the lower covering factor for the other components. However, apart from the UV–X-ray absorber they all inclined to f_c equal to 1. Due to changes of the covering factor through the observations and the fact that high velocities placed it to be the closest absorber to the source (Ebrero *et al.* 2016), another approach was needed.

The varying covering factor of the obscuring absorber can cause additional variations of the flux seen by the more distant absorbers. Therefore, new modified SEDs including the absorption of the first absorber have been produced to incorporate this fact. New photoionisation balance was calculated and fed to the other more distant absorbers.

We started out the fit again with the obscuring UV–X-ray absorber. This resulted in a big improvement of the fit compared to the model with continuum components through all the observations. We continued adding *xabs* components with 4 free parameters and the newly calculated ionisation balance as input to *xabs*. We repeated the process until no significant improvement of the fit was registered.

For the observations 2003 and 2013, we found the UV–X-ray obscurer plus 2 significant warm absorbers. There is also a hint of another highly ionised warm absorber as reported by Krongold *et al.* (2008). The high-quality observations from 2015 revealed additional 2

	Obs. 2003		Obs. 2013	
Model	C-stat	$\log\xi$	C-stat	$\log\xi$
0wa	872.06	-	805.26	-
1wa	686.93	**-0.8**	599.08	**-0.8**
2wa	527.99	2.31, **-0.8**	511.39	2.19, **-0.8**
<u>3wa</u>	<u>513.19</u>	2.42, 1.85, **-0.8**	<u>496.90</u>	2.20, 1.67, **-0.8**
4wa	505.71	2.92, 1.96, 1.43, **-0.8**	491.73	2.50, 2.19, 1.64, **-0.8**
	Obs. 2015a		Obs. 2015b	
Model	C-stat	$\log\xi$	C-stat	$\log\xi$
0wa	2935.45	-	3533.31	-
1wa	2332.08	**-0.8**	2915.31	**-0.8**
2wa	1269.47	2.06, **-0.8**	1411.69	2.06, **-0.8**
3wa	1107.21	2.72, 1.95, **-0.8**	1184.96	2.80, 1.97, **-0.8**
4wa	1063.82	2.78, 2.70, 1.96, **-0.8**	1152.40	2.92, 2.87, 1.98, **-0.8**
<u>5wa</u>	<u>1045.81</u>	2.81, 2.59, 2.01, 1.59, **-0.8**	<u>1093.21</u>	2.94, 2.92, 2.03, 1.45, **-0.8**

Table 4.5: Progress of the fit after each iteration of the inclusion of additional warm absorber component.

warm absorbers, putting the total count to 4 warm absorbers plus 1 obscurer. All data with the improvement of the fit are provided in table 4.5. Figures 4.9, 4.10, 4.11 display the combined RGS spectra with the fitted model while the table 4.6 shows the best-fit values of the warm absorber parameters. The order of warm absorbers was constructed considering the best-fit values of outflow velocities, column densities and ionisation level parameters from the fit. However, due to high error bars in these parameters, especially in archive 2003 and 2013 observations, we recommend taking this order with caution.

The covering factor of the first UV–X-ray absorber is changing within the observations significantly. In the observation 2013, it covers the source fully. This can be considered as the main reason why we observed a drop of flux in X-rays. In the newest data, the flux is getting to the previous levels and the covering factor of this absorber also drops down to lower values.

The results also show the presence of high-velocity component $Xabs$ 2 that appeared in the data of 2013 observation with the outflow velocity of $\sim$ 7000 km s^{-1} and ionisation level of $\log(\xi) = 2.2$ erg cm s^{-1}. We detect other high-velocity warm absorber again in the new high-quality data of 2015's observations, wherein the period of 2 years it either slowed down and got more ionised or we observe different warm absorber. High velocities of this component could mean that the warm absorber is positioned somewhere close to the broad line region.

Model	Parameter	Obs. 2003	Obs. 2013	Obs. 2015A	Obs. 2015B
Xabs 1	nh	$2.17^{+0.99}_{-0.59} \times 10^{22}$	$3.49^{+0.68}_{-0.52} \times 10^{22}$	$2.72^{+0.91}_{-0.55} \times 10^{22}$	$1.8^{+1.3}_{-0.7} \times 10^{22}$
	f_c	$0.64^{+0.13}_{-0.09}$	$0.98^{+0.01}_{-0.02}$	$0.47^{+0.06}_{-0.09}$	$0.15^{+0.10}_{-0.06}$
	$\log \xi$	**-0.8**	**-0.8**	**-0.8**	**-0.8**
	σ	**600**	**600**	**600**	**600**
	v_{out}	**-6000**	**-6000**	**-6000**	**-6000**
Xabs 2	nh		$1.29^{+0.49}_{-0.35} \times 10^{22}$	$1.18^{+2.7}_{-0.6} \times 10^{22}$	$3.7^{+2.4}_{-1.8} \times 10^{22}$
	$\log \xi$		$2.200^{+0.004}_{-0.008}$	$2.81^{+0.03}_{-0.07}$	$2.94^{+0.02}_{-0.03}$
	σ	...	41^{+35}_{-18}	64^{+45}_{-40}	4^{+14}_{-4}
	v_{out}		-7144^{+142}_{-251}	-5107^{+97}_{-108}	-5117^{+63}_{-44}
Xabs 3	nh	$2.4^{+2.0}_{-1.5} \times 10^{22}$		$3.2^{+1.5}_{-1.2} \times 10^{22}$	$9.2^{+6.6}_{-3.4} \times 10^{22}$
	$\log \xi$	$2.42^{+0.08}_{-0.14}$		$2.59^{+0.11}_{-0.06}$	$2.92^{+0.02}_{-0.02}$
	σ	59^{+111}_{-34}	...	16^{+12}_{-11}	27^{+12}_{-14}
	v_{out}	-204^{+118}_{-337}		-691^{+51}_{-36}	-650^{+37}_{-25}
Xabs 4	nh	$8.8^{+2.1}_{-2.1} \times 10^{21}$	$1.68^{+0.62}_{-0.53} \times 10^{21}$	$5.58^{+0.59}_{-0.69} \times 10^{21}$	$5.96^{+0.43}_{-0.37} \times 10^{21}$
	$\log \xi$	$1.85^{+0.03}_{-0.04}$	$1.67^{+0.16}_{-0.20}$	$2.01^{+0.04}_{-0.02}$	$2.03^{+0.02}_{-0.02}$
	σ	66^{+38}_{-25}	73^{+61}_{-44}	103^{+22}_{-20}	128^{+14}_{-15}
	v_{out}	-386^{+219}_{-179}	-21^{+277}_{-355}	-354^{+44}_{-41}	-339^{+33}_{-27}
Xabs 5	nh			$9.5^{+6.8}_{-3.9} \times 10^{20}$	$1.06^{+0.24}_{-0.22} \times 10^{21}$
	$\log \xi$			$1.59^{+0.14}_{-0.15}$	$1.46^{+0.08}_{-0.09}$
	σ	...	...	67^{+52}_{-32}	78^{+32}_{-25}
	v_{out}			-550^{+81}_{-62}	-557^{+72}_{-72}
C-stat/D.O.F.		513/403	497/388	1046/863	1093/863

Table 4.6: Warm Absorbers best-fit values with 1σ errors of parameters column density nH [cm^{-2}], ionisation ξ [erg cm s^{-1}], velocity dispersion σ [km s^{-1}], outflow velocity v_{out} [km s^{-1}] and covering factor f_c. D.O.F - Degrees of Freedom **Bold** values are adopted from the UV data (Ebrero *et al.* 2016).

4.4.3 Stability curve

In this part of our analysis, we took the data produced by photoionisation code CLOUDY and created the stability curves of NGC 985 using equation 1.5 for each case of the modified obscured SED. We then took the best-fit values of the model and after transforming ionisation parameters overplotted them on top of the S-curve.

Stability curve of this source can be divided into two regions (as mentioned in section 1.4). The stable part of the curve, where the slope is positive, contains 3 studied warm absorbers, *Xabs* 1, 4 and 5. Therefore, their position on the curve will probably not change significantly in time. On the other hand warm absorbers *xabs* 2 and 3 lie in the unstable region of the curve, where the slope is negative. They are both moving within the unstable region of the curve throughout the observations.

There are also regions of the curve, where the pressure equilibrium allows multiphase nature of the warm absorber to occur. In the case of observation 2013 both of the warm absorbers lie in the same pressure range. This could suggest the existence of one structure with two distinct ionisation phases. However, in this case outflow velocities differ by a factor of ten, hence the multiphase structure is highly improbable.

In the observation 2015, all absorbers could be marginally considered to lie in the pressure equilibrium. Nevertheless, deriving the multiphase nature solely by the stability curves shown in figure 4.8 has to be taken with huge caution. There are factors within AGNs, like magnetic fields, that are not taken into account by the CLOUDY calculations. Nonetheless,
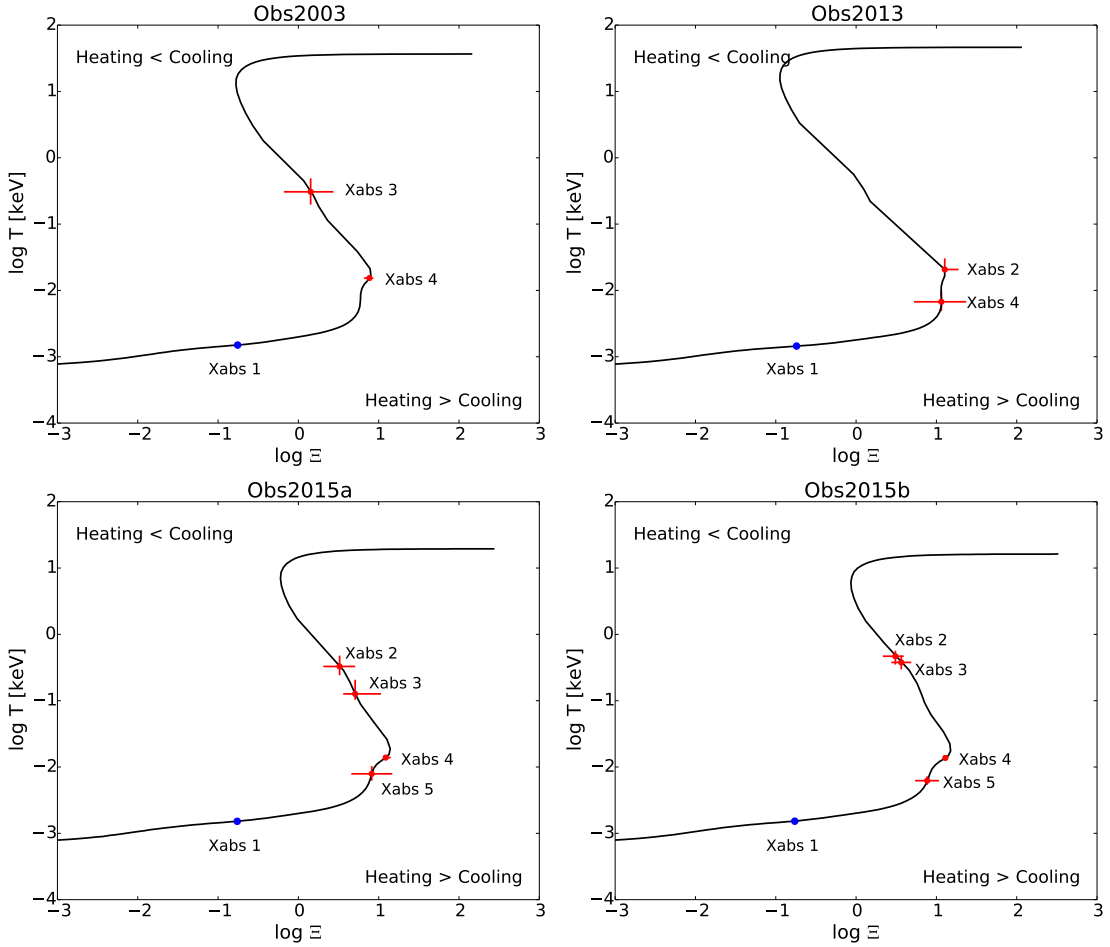

Figure 4.8: Stability curves with the warm absorbers **Top** archive observations from 2003 and 2013 **Bottom** recent observations form 2015.

it is a useful tool to see how changes of the flux affect the warm absorber and its movement in this phase diagram.

We note, that the absence of the *xabs* components 2, 3 and 5 in the archive 2003 and 2013 data does not mean they were not there before. The reason of their non-occurrence might be caused by the lower quality of the data preventing their significant detection.
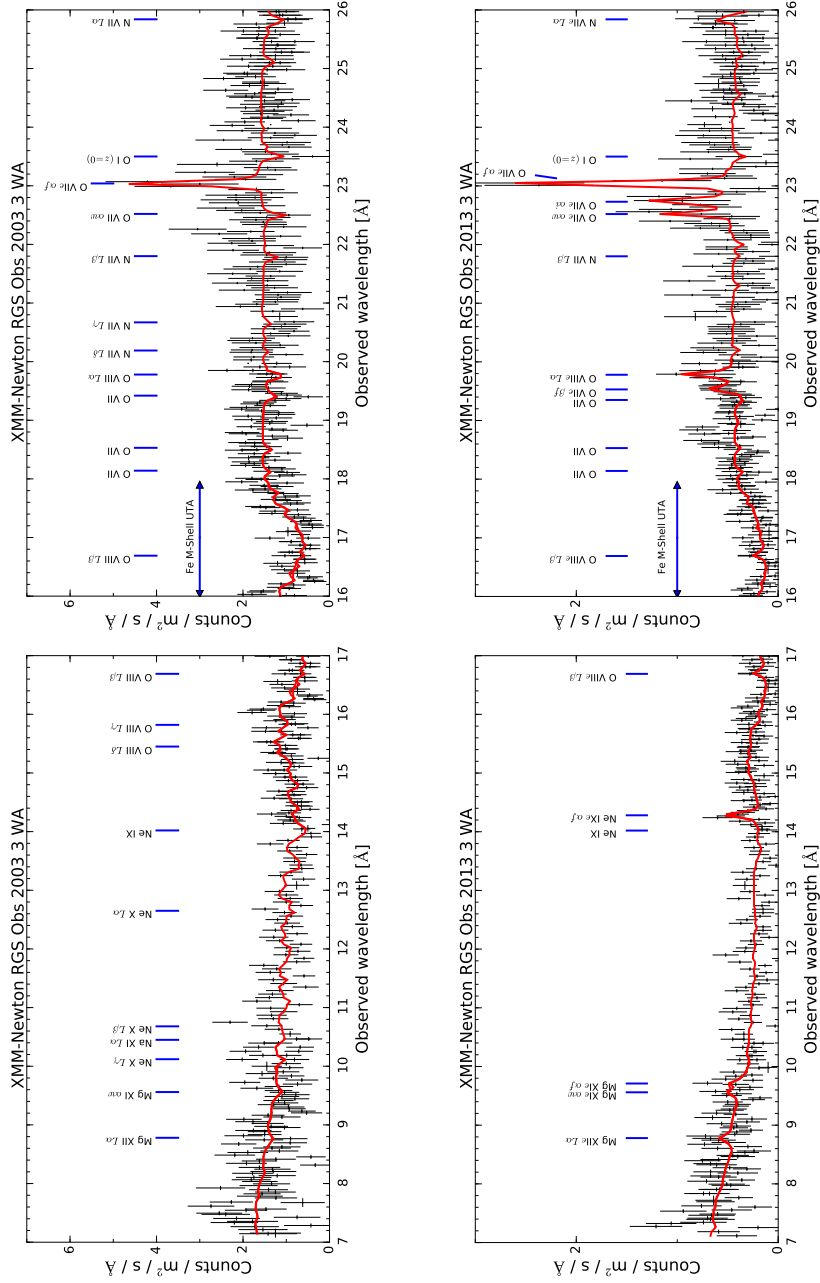
Figure 4.9: Final fitted model overlayed on the combined RGS spectra. **Top** observation 2003 **Bottom** observation 2013.
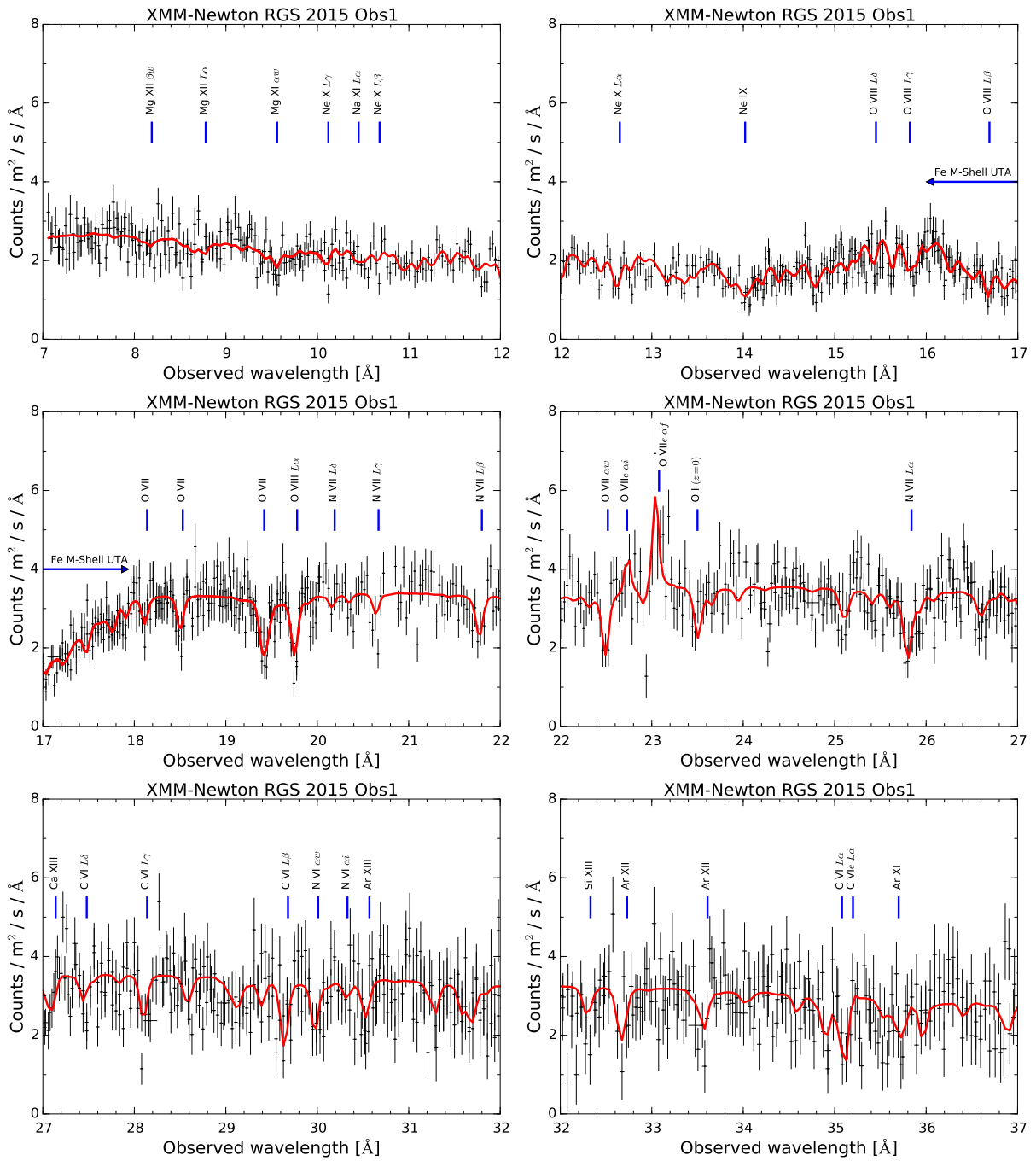
Figure 4.10: Final fitted model overlayed on the combined RGS spectra of the observation 2015a.
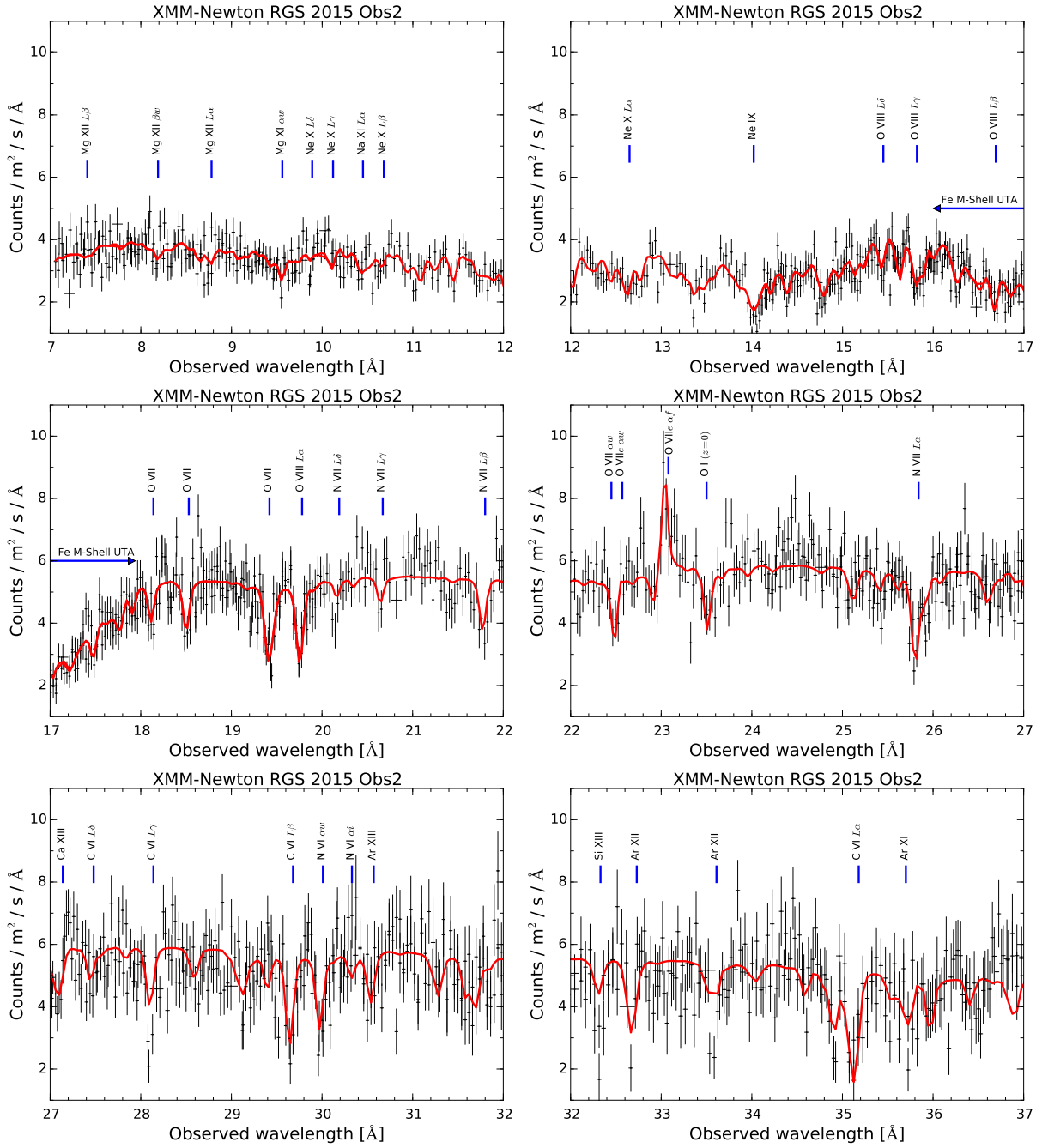
Figure 4.11: Final fitted model overlayed on the combined RGS spectra of the observation 2015b.

Chapter 5

Discussion and Conclusions

In the first part of our work, we studied the effects of both the lamp-post geometry and the radially stratified ionisation profile of the accretion disc on the radial-emissivity index. We conducted a systematic analysis to explore a large range of the parameter space and thus significantly extend the work present in Svoboda *et al.* (2012). We investigated different ionisation profiles through assumptions of the disc densities ranging between 10^{14} and 10^{19} cm^{-3}. The higher the density is, the less the disc gets ionised when subjected to the same illuminating flux. For each ionisation profile of the disc, we performed the simulations of the corona being at different heights, ranging between 1.5 and 9 r_g above the black hole.

We found out that assumption of the constant ionisation disc applied on the data with the radially-stratified ionisation (as could be expected in the real accretion disc) can significantly affect the measured values of the radial-emissivity. When such a constant-ionisation model is used, the ionisation in the innermost parts of the disc is largely underestimated by the fit which transfers into the measured steeper radial-emissivity index q. Our analysis shows, that for a ionised disc with a large ionisation gradient the radial-emissivity index reaches for the low heights of the corona values up to $q \sim 7$. As the corona gets higher, more radiation extends to the outer parts of the disc and the emissivity profile gets flatter. For the cases when the disc is either too cold or too hot, the ionisation profile differences between the parts of the disc are small enough and therefore only the height of the corona affects the steepness of q. For these conditions we measured $q \sim 4$–5 which is in agreement with the previous findings (Dovčiak *et al.* 2014; Svoboda *et al.* 2012; Wilkins & Fabian 2012).

Using the more evolved models accounting for the radially stratified ionisation profile should, therefore, give us a more realistic view of the conditions prevailing in the vicinity of the black holes. This is especially important when the other physical parameters such as the spin of the black hole and properties of the X-ray irradiating corona are deduced

by these reflection models.

In the analysis we employed three different X-ray detectors, one from the ESA's currently largest X-ray observatory XMM-Newton and two from the future missions Nicer and Athena. Differences between individual detectors are visible mainly in the lower standard errors of the parameters and greater reduced χ^2 of the fit for the future planned detectors. This shows that future missions will be better equipped to more precisely constrain model parameters and the more complex and developed astrophysical models will be needed to fit properly the future data.

In addition, comparison of the relativistic blurring models *Kyconv*, *Relconv* and most commonly used *Kdblur2* shows differences in the steepness of the radial-emissivity achieved by the individual models. The differences are both in the effects of the lamp-post geometry and density of the disc. Even though the general results of the radially stratified ionisation causing steeper radial-emissivity measurements stay unchanged, this divergence in the values fitted by the different models is interesting and more investigation of this matter will be needed.

We also investigated the connection between the two studied parameters, ionisation ξ and radial-emissivity index q, by creating the contour maps between them. They show apparent degeneracy between the two parameters. This degeneracy may play a significant role in the determination of the radial-emissivity index in the fitting model depending on the value of average ionisation obtained during the fit.

All gathered results will be part of the prepared publication (Domček, Svoboda & Dovčiak, in prep.).

The second part of the work concentrates on the analysis of the high-resolution X-ray spectra of the active galaxy NGC 985. We specifically study the presence of absorption features caused by the outflowing gas intrinsic to the active galaxy, known as warm absorbers. The analysis is done for the two archive (2003, 2013) and two recent (2015) XMM-Newton observations with longer exposure that allowed for detailed high-resolution X-ray spectroscopy.

In the archive observations, we were able to significantly detect 3 warm absorbers, while the new, high-quality data showed 5 of them to be present. This is one more detection compared to the simultaneous EPIC-PN detector observation (Ebrero *et al.* 2016) and two more than in any previous observation done for this source (Krongold *et al.* 2005, 2008; Parker *et al.* 2014). In addition, one of the absorbers is characterised by low ionisation parameter $\log(\xi) = -0.8$ and is seen both in UV and X-ray data (Ebrero *et al.* 2016).

This special UV–X-ray absorber is causing obscuration of the source in the soft X-rays in all four observations. In 2013 data, we see the maximum of the obscuration (compared to the past unobscured observations) with the drop of soft X-ray (0.2–2.0 keV) flux by

more than the order of magnitude, while in the hard X-rays (2–10 keV) the flux changes only by a factor of 2 or 3. In 2015, the obscuration diminishes greatly returning the flux almost back to the long-term maxima.

The Swift X-ray observatory observed the source in 2013 during the drop of flux in the monitoring programme. The data showed that the eclipsing event lasted at least 40 days (Parker *et al.* 2014). It is therefore possible that in our 2015 data, we observed the end of this eclipsing event. Moreover, we see signs of partial X-ray obscuration also in the 2003 data. This is very interesting due to observed high flux in the other Swift monitoring programme from 2007–2008 (Parker *et al.* 2014). It is plausible that the eclipsing event in 2003 data is different one to the one observed in the 2013-2015 time period.

Broad observed lines and high outflow velocities of both mentioned obscurers suggest the position in or very near the broad line region. One plausible scenario of the origin of the BLR clouds proposed by Czerny & Hryniewicz (2011) suggests that these clouds originate in the dustier part of the accretion disc and the clouds are repeatedly formed and destroyed by the ionising flux from the source. This theory could explain how we can observe two eclipsing events with similar warm absorber properties.

We also detect one high-velocity component in both 2013 and 2015 data. However, the newer data show higher ionisation and lower outflow velocity than the previous. The absorber, therefore, either slowed down and got more ionised or we observe totally different absorbing cloud. High outflow velocities (whether it is one or two different absorbers) suggest the location in the inner part of the narrow line region.

Other warm absorbers show lower ionisation and velocities dispersion of the lines characteristic to the narrow line region. We also report that apart from the UV–X-ray absorber all of them could be marginally considered to be in the pressure equilibrium with each other. The study of the variability of the warm absorber properties in response to the ionising flux could also give constraints on the more precise locations. However, that is beyond the scope of this thesis and will be done in the upcoming paper (Ebrero & Domček et al., in prep.). One possible view of the system based on the results in the table 4.6 is shown in figure 5.1.

As a byproduct of our analysis, we found in the spectra several H-like and He-like emission lines such as O VII, O VIII, Ne IX and more. As a possible extension of this work, these lines could be investigated through the plasma diagnostics tools to constrain the electron temperature and cloud density in the place of their origin.

NGC 985 is also known to be the case of galaxy merger with two distinguishable cores 2–3 kpc apart (Appleton & Marcum 1993). However, if the second core was active, double-peaked emission lines would be detected. Because there is no evidence for it, we conclude that our data contain X-ray emission only from one active core.

Future observations of this source could provide more information on the properties of

X-ray warm absorbers and their connection to the absorbers seen in the UV domain and finally their common origin. Two long-term eclipsing events causing the drop of the soft X-ray flux were already reported and more obscuration events may be detected with future observations. NGC 985 therefore represents an interesting source for further studies.
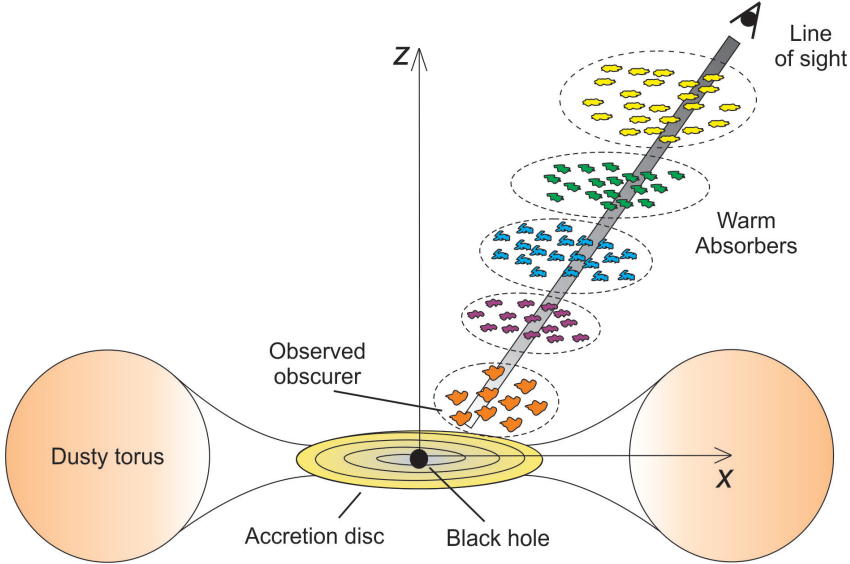

Figure 5.1: Schematic picture of the NGC 985 system with warm absorbers. X-ray radiation from the central source is absorbed by the warm clouds resulting in the observed absorption features in the spectra. Individual absorbers can have a clumpy structure consisting of multiple clouds with the same properties.

Bibliography

Ahn, C. P., Alexandroff, R., Allende Prieto, C., et al. (2012). *The Astrophysical Journal Supplement Series*, **203**(2), 21. 43

Antonucci, R. (1993). *Annual Review of Astronomy and Astrophysics*, **31**(1), 473–521. 11

Antonucci, R. R. J. & Miller, J. S. (1985). *The Astrophysical Journal*, **297**, 621. 11, 19

Appleton, P. N. & Marcum, P. M. (1993). *The Astrophysical Journal*, **417**, 90. 43, 61

Arav, N. (2002). AGN Outflows: Analysis of the Absorption Troughs. In *X-ray Spectroscopy of AGN with Chandra and XMM-Newton*, page 153. 42

Arnaud, K. A. (1996). XSPEC: The First Ten Years. In *Astronomical Data Analysis Software and Systems V*, volume 101, page 17. 31

Arribas, S., Mediavilla, E., del Burgo, C., & Garcia Lorenzo, B. (1999). *The Astrophysical Journal*, **511**(2), 680–685. 42, 48

Beckmann, V. & Shrader, C. R. (2012). *Active galactic nuclei*. Wiley-VCH. 14

Behar, E., Rasmussen, A. P., Blustin, A. J., et al. (2003). *The Astrophysical Journal*, **598**(1), 232–241. 18

Bergmann, T. S. (2014). *Proceedings of the International Astronomical Union*, **10**(S309), 190–195. 17

Bianchi, S., Maiolino, R., & Risaliti, G. (2012). *Advances in Astronomy*, **2012**, 1–17. 19

Blandford, R. D. & McKee, C. F. (1982). *The Astrophysical Journal*, **255**, 419. 17, 24

Blustin, A. J., Page, M. J., Fuerst, S. V., Branduardi Raymont, G., & Ashton, C. E. (2005). *Astronomy and Astrophysics*, **431**(1), 111–125. 18

Brandt, W. N., Fabian, A. C., Nandra, K., Reynolds, C. S., & Brinkmann, W. (1994). *Monthly Notices of the Royal Astronomical Society*, **271**(4), 958–966. 42

Bridle, A. H., Hough, D. H., Lonsdale, C. J., Burns, J. O., & Laing, R. A. (1993). "Tired" Jets in Extended 3CR Quasars. In *Bulletin of the American Astronomical Society*, volume 25, page 1418. 12

Burtscher, L., Jaffe, W., Raban, D., et al. (2009). *The Astrophysical Journal*, **705**(1), L53–L57. 20

Cardelli, J. A., Clayton, G. C., & Mathis, J. S. (1989). *The Astrophysical Journal*, **345**, 245. 47

Cash, W. (1979). *The Astrophysical Journal*, **228**, 939. 49

Chakravorty, S., Kembhavi, A. K., Elvis, M., & Ferland, G. (2009). *Monthly Notices of the Royal Astronomical Society*, **393**(1), 83–98. 23

Chakravorty, S., Misra, R., Elvis, M., Kembhavi, A. K., & Ferland, G. (2012). *Monthly Notices of the Royal Astronomical Society*, **422**(1), 637–651. 22

Chartas, G., Rhea, C., Kochanek, C., et al. (2015). *Astronomische Nachrichten.* 28

Crenshaw, D. M., Kraemer, S. B., Boggess, A., et al. (1999). *The Astrophysical Journal*, **516**(2), 750–768. 19

Czerny, B. & Hryniewicz, K. (2011). *Astronomy & Astrophysics*, **525**, L8. 18, 61

Dai, X., Kochanek, C. S., Chartas, G., et al. (2009). *The Astrophysical Journal*, **709**(1), 278–285. 28

Dauser, T., Wilms, J., Reynolds, C. S., & Brenneman, L. W. (2010). *Monthly Notices of the Royal Astronomical Society*, **409**(4), 1534–1540. 31

Dauser, T., Garcia, J., Wilms, J., et al. (2013). *Monthly Notices of the Royal Astronomical Society*, **430**(3), 1694–1708. 31

de Vaucouleurs, G. & de Vaucouleurs, A. (1975). *The Astrophysical Journal*, **197**, L1. 42

Dovčiak, M., Karas, V., Martocchia, A., Matt, G., & Yaqoob, T. (2004). An XSPEC model to explore spectral features from black-hole sources. In *Processes in the vicinity of black holes and neutron stars.* 31

Dovčiak, M., Muleri, F., Goosmann, R. W., Karas, V., & Matt, G. (2011). *The Astrophysical Journal*, **731**(1), 75. 28

Dovčiak, M., Svoboda, J., Goosmann, R. W., et al. (2014). An XSPEC model to explore spectral features from black-hole sources - II. The relativistic iron line in the lamp-post geometry. In *RAGtime 12 - workshop on black holes and neutron stars*. 29, 31, 59

Dullemond, C. P. & van Bemmel, I. M. (2005). *Astronomy and Astrophysics*, **436**(1), 47–56. 19

Ebrero, J., Kriss, G. A., Kaastra, J. S., & Ely, J. C. (2016). *Astronomy & Astrophysics*, **586**, A72. 43, 47, 48, 49, 51, 53, 60

Edge, D. O., Shakeshaft, J. R., McAdam, W. B., Baldwin, J. E., & Archer, S. (1959). *Memoirs of the Royal Astronomical Society*, **68**, 37–60. 12

Elvis, M. (2000). *The Astrophysical Journal*, **545**(1), 63–76. 18

Elvis, M., Maccacaro, T., Wilson, A. S., et al. (1978). *Monthly Notices of the Royal Astronomical Society*, **183**(2), 129–157. 12

Elvis, M., Risaliti, G., Nicastro, F., et al. (2004). *The Astrophysical Journal*, **615**(1), L25–L28. 17

Fabian, A. C., Rees, M. J., Stella, L., & White, N. E. (1989). *Monthly Notices of the Royal Astronomical Society*, **238**(3), 729–736. 16, 24

Fabian, A. C., Vaughan, S., Nandra, K., et al. (2002). *Monthly Notices of the Royal Astronomical Society*, **335**(1), L1–L5. 25, 32

Fabian, a. C., Zoghbi, A., Ross, R. R., et al. (2009). *Nature*, **459**, 540. 24

Fabian, A. C., Wilkins, D. R., Miller, J. M., et al. (2012). *Monthly Notices of the Royal Astronomical Society*, **424**(1), 217–223. 25

Ferland, G. J., Porter, R. L., van Hoof, P. A. M., et al. (2013). The 2013 Release of Cloudy. 21, 47

Gabriel, C., Hoar, J., Ibarra, A., et al. (2004). The XMM-Newton SAS -Distributed Development and Maintenance of a Large Science Analysis System: A Critical Analysis. In *Astronomical Data Analysis Software and Systems (ADASS) XIII*, volume 314, page 759. 45

Garcia, A. M. P. & Espinosa, J. M. R. (1996). *The Astronomical Journal*, **112**, 1863. 42

Gendreau, K. C., Arzoumanian, Z., & Okajima, T. (2012). No Title. In T. Takahashi, S. S. Murray & J.-W. A. den Herder, editors, *Space Telescopes and Instrumentation 2012: Ultraviolet to Gamma Ray*, volume 8443, page 844313. 33

Halpern, J. P. (1984). *The Astrophysical Journal*, **281**, 90. 18

Heckman, T. M. (1980). *Astronomy and Astrophysics*, **87**, 152–164. 12

Jaffe, W., Meisenheimer, K., Röttgering, H. J. A., et al. (2004). *Nature*, **429**(6987), 47–49. 20

Jansen, F., Lumb, D., Altieri, B., et al. (2001). *Astronomy and Astrophysics*, **365**(1), L1–L6. 44

Kaastra, J. S. & Barr, P. (1989). *Astronomy and Astrophysics*, **226**, 59–68. 49

Kaastra, J. S., Mewe, R., & Nieuwenhuijzen, H. (1996). *UV and X-ray Spectroscopy of Astrophysical and Laboratory Plasmas*, pages 411–414. 49

Kaastra, J. S., Raassen, A. J. J., Mewe, R., et al. (2004). *Astronomy and Astrophysics*, **428**(1), 57–66. 18

Kaspi, S., Maoz, D., Netzer, H., et al. (2005). *The Astrophysical Journal*, **629**(1), 61–71. 17

Kellermann, K. I., Sramek, R., Schmidt, M., Shaffer, D. B., & Green, R. (1989). *The Astronomical Journal*, **98**, 1195. 10

Khachikian, E. Y. & Weedman, D. W. (1971). *The Astrophysical Journal*, **164**, L109. 11

Khachikian, E. Y. & Weedman, D. W. (1974). *The Astrophysical Journal*, **192**, 581. 11

Krolik, J. H. & Kriss, G. A. (2001). *The Astrophysical Journal*, **561**(2), 684–690. 18

Krongold, Y., Nicastro, F., Brickhouse, N. S., et al. (2003). *The Astrophysical Journal*, **597**(2), 832–850. 18

Krongold, Y., Nicastro, F., Elvis, M., et al. (2005). *The Astrophysical Journal*, **620**(1), 165–182. 18, 42, 43, 60

Krongold, Y., Nicastro, F., Elvis, M., et al. (2007). *The Astrophysical Journal*, **659**(2), 1022–1039. 18

Krongold, Y., Jimenez-Bailon, E., Santos-Lleo, M., et al. (2008). *The Astrophysical Journal*, **690**(1), 773–782. 43, 51, 60

Laor, A. (1991). *The Astrophysical Journal*, **376**, 90. 31

Liu, B. F. & Mineshige, S. (2002). Accretion Disk Corona in AGN. In *8th Asian-Pacific Regional Meeting, Volume II*, pages 391–392. 16

Liu, B. F., Mineshige, S., & Ohsuga, K. (2003). *The Astrophysical Journal*, **587**(2), 571–579. 16

Longair, M. S. & Malcolm S. Longair (2011). *High Energy Astrophysics, 3rd edn., by Malcolm S. Longair*. Cambridge University press. 11, 12, 13

Lynden-Bell, D. & Pringle, J. E. (1974). *Monthly Notices of the Royal Astronomical Society*, **168**(3), 603–637. 16

MacLeod, J. M. & Andrew, B. H. (1968). *Astrophysical Letters*, **1**, 243. 13

Maiolino, R., Risaliti, G., Salvati, M., et al. (2010). *Astronomy and Astrophysics*, **517**, A47. 17

Martocchia, A. & Matt, G. (1996). *Monthly Notices of the Royal Astronomical Society*, **282**, L53–L57. 27

Mathur, S., Elvis, M., & Wilkes, B. (1995). *The Astrophysical Journal*, **452**, 230. 19

Mathur, S., Wilkes, B., & Elvis, M. (1998). *The Astrophysical Journal*, **503**(1), L23–L26. 19

Matt, G., Perola, G. C., & Piro, L. (1991). *Astronomy and Astrophysics*, **247**, 25–34. 27

McHardy, I. M., Gunn, K. F., Uttley, P., & Goad, M. R. (2005). *Monthly Notices of the Royal Astronomical Society*, **359**(4), 1469–1480. 32

Miller, J. (2007). *Annual Review of Astronomy and Astrophysics*, **45**(1), 441–479. 25

Miller, J. S. (1994). The Unification of Active Galaxies: Seyferts and Beyond. In *The Physics of Active Galaxies*, volume 54, page 149. 11

Miniutti, G., Fabian, A. C., Anabuki, N., et al. (2007). *Publications of the Astronomical Society of Japan*, **59**(sp1), S315–S325. 25

Misner, C. W., Thorne, K. S., & Wheeler, J. A. (1973). *Gravitation*. W. H. Freeman. 15

Murray, N., Chiang, J., Grossman, S. A., & Voit, G. M. (1995). *The Astrophysical Journal*, **451**, 498. 18

Mushotzky, R. F., Done, C., & Pounds, K. A. (1993). *Annual Review of Astronomy and Astrophysics*, **31**(1), 717–761. 16

Netzer, H. (2006). Active Galactic Nuclei: Basic Physics and Main Components. In *Physics of Active Galactic Nuclei at all Scales*, volume 693, pages 1–38. Springer Berlin Heidelberg. 16, 17

Netzer, H. (2013). *The Physics and Evolution of Active Galactic Nuclei, by Hagai Netzer, Cambridge, UK: Cambridge University Press, 2013*. 18

Netzer, H. (2015). *Annual Review of Astronomy and Astrophysics*, **53**(1), 365–408. 20

Netzer, H., Kaspi, S., Behar, E., et al. (2003). *The Astrophysical Journal*, **599**(2), 933–948. 18

Nicastro, F. (2000). *The Astrophysical Journal*, **530**(2), L65–L68. 12

Nicastro, F., Fiore, F., Perola, G. C., & Elvis, M. (1999). *The Astrophysical Journal*, **512**(1), 184–196. 22, 42

Nicastro, L., Amati, L., Antonelli, L. A., et al. (1998). *Astronomy and Astrophysics*, **338**, L17–L20. 42

Novikov, I. D. & Thorne, K. S. (1973). Astrophysics of black holes. 16

Osterbrock, D. E. & Koski, A. T. (1976). *Monthly Notices of the Royal Astronomical Society*, **176**(1), 61P–66P. 11

Parker, M. L., Schartel, N., Komossa, S., et al. (2014). *Monthly Notices of the Royal Astronomical Society*, **445**(1), 1039–1047. 43, 60, 61

Pérez Beaupuits, J. P., Wada, K., & Spaans, M. (2011). *The Astrophysical Journal*, **730**(1), 48. 17

Peterson, B. M. (1993). *Publications of the Astronomical Society of the Pacific*, **105**, 247. 17

Pier, E. A. & Krolik, J. H. (1992). *The Astrophysical Journal*, **401**, 99. 19

Ponti, G., Gallo, L. C., Fabian, A. C., et al. (2010). *Monthly Notices of the Royal Astronomical Society*, **406**(4), 2591–2604. 25

Porquet, D. & Dubau, J. (2000). *Astronomy and Astrophysics Supplement Series*, **143**(3), 495–514. 20, 21

Pounds, K. A., Reeves, J. N., Page, K. L., et al. (2003). *Monthly Notices of the Royal Astronomical Society*, **341**(3), 953–960. 18

Pringle, J. E. (1981). *Annual Review of Astronomy and Astrophysics*, **19**(1), 137–160. 16

Puccetti, S., Fiore, F., Risaliti, G., et al. (2007). *Monthly Notices of the Royal Astronomical Society*, **377**(2), 607–616. 17

Raban, D., Jaffe, W., Röttgering, H., Meisenheimer, K., & Tristram, K. R. W. (2009). *Monthly Notices of the Royal Astronomical Society*, **394**(3), 1325–1337. 20

Ravera, L., Barret, D., Willem Den Herder, J., et al. (2014). The X-ray Integral Field Unit (X-IFU) for Athena. In T. Takahashi, J.-W. A. den Herder & M. Bautz, editors, *Space Telescopes and Instrumentation 2014: Ultraviolet to Gamma Ray*, volume 9144, page 91442L. 33

Reeves, J., Pounds, K., Nandra, K., et al. (2004). High velocity X-ray outflows in Active Galactic Nuclei. In *35th COSPAR Scientific Assembly*, volume 35, page 3660. 18

Reynolds, C. & Nowak, M. A. (2003). *Physics Reports*, **377**(6), 389–466. 16

Reynolds, C. S. & Begelman, M. C. (1997). *The Astrophysical Journal*, **488**(1), 109–118. 25

Risaliti, G., Bianchi, S., Matt, G., et al. (2005). *The Astrophysical Journal*, **630**(2), L129–L132. 17

Risaliti, G., Elvis, M., Fabbiano, G., et al. (2007). *The Astrophysical Journal*, **659**(2), L111–L114. 17

Risaliti, G., Miniutti, G., Elvis, M., et al. (2009). *The Astrophysical Journal*, **696**(1), 160–171. 17

Risaliti, G., Harrison, F. A., Madsen, K. K., et al. (2013). *Nature*, **494**(7438), 449–451. 28

Różańska, A., Goosmann, R., Dumont, A.-M., & Czerny, B. (2006). *Astronomy and Astrophysics*, **452**(1), 1–13. 18

Schmidt, M. (1963). *Nature*, **197**(4872), 1040–1040. 12

Schmidt, M. (1969). *Annual Review of Astronomy and Astrophysics*, **7**(1), 527–552. 12

Seyfert, C. K. (1943). *The Astrophysical Journal*, **97**, 28. 10

Shakura, N. I. & Sunyaev, R. a. (1973). *Astronomy and Astrophysics*, **24**, 337–355. 16, 25

Sochora, V., Karas, V., Svoboda, J., & Dovčiak, M. (2011). *Monthly Notices of the Royal Astronomical Society*, **418**(1), 276–283. 26

Stalevski, M., Fritz, J., Baes, M., Nakos, T., & Popović, L. Č. (2012). *Monthly Notices of the Royal Astronomical Society*, **420**(4), 2756–2772. 20

Stein, W. A. (1978). *BL Lac Objects*, pages 1–19. 13

Strüder, L., Briel, U., Dennerl, K., et al. (2001). *Astronomy and Astrophysics*, **365**(1), L18–L26. 33

Svoboda, J., Dovčiak, M., Goosmann, R. W., & Karas, V. (2009). Comparison of Relativistic Iron Line Models. In *Week of Doctoral Students 2008 - Proceedings of Contributed Papers*, pages 204–212. MATFYZPRESS. 32

Svoboda, J., Dovčiak, M., Goosmann, R. W., et al. (2012). *Astronomy & Astrophysics*, **545**, A106. 30, 59

Tanaka, Y., Nandra, K., Fabian, A. C., et al. (1995). *Nature*, **375**(6533), 659–661. 16

Tran, H. D. (2001). *The Astrophysical Journal*, **554**(1), L19–L23. 12

Tran, H. D. (2003). *The Astrophysical Journal*, **583**(2), 632–648. 12

Tristram, K. R. W., Meisenheimer, K., Jaffe, W., et al. (2007). *Astronomy and Astrophysics*, **474**(3), 837–850. 19, 20

Ulrich, M. H., Boksenberg, A., Bromage, G. E., et al. (1984). *Monthly Notices of the Royal Astronomical Society*, **206**(1), 221–237. 11

Vaughan, S. & Fabian, A. C. (2004). *Monthly Notices of the Royal Astronomical Society*, **348**(4), 1415–1438. 24

Wang, L. & Cen, R. (2016). *The Astrophysical Journal*, **817**(2), 99. 16

Wilkins, D. R. & Fabian, A. C. (2011). *Monthly Notices of the Royal Astronomical Society*, **414**(2), 1269–1277. 25, 26

Wilkins, D. R. & Fabian, A. C. (2012). *Monthly Notices of the Royal Astronomical Society*, **424**(2), 1284–1296. 25, 59

Wilkins, D. R. & Gallo, L. C. (2015). *Monthly Notices of the Royal Astronomical Society*, **21**(January), 1–21. 26, 28

Woltjer, L. (1959). *Astrophysical Journal*, **130**(07), 38. 10

Appendix

Kyreflionx model parameters

Parameter	Definition and possible values
par 1	the black hole angular momentum ($0 \leq a/M \leq 1$)
par 2	the observer inclination in degrees ($0°$ - pole, $90°$ - disc)
par 3	the inner edge of an accretion disc in GM/c^2 ($1 \leq r_{out} \leq 1000$)
par 4	0 - means integration from the disc inner edge, par3
	1 - if par3 is bellow ISCO, integration is done above ISCO only
par 5	the outer edge of an accretion disc in GM/c^2 ($1 \leq r_{out} \leq 1000$)
par 6	the mass of the black hole in 10^8 $M_\odot$ ($10^{-8} \leq M \leq 10^3$)
par 7	the height of the primary source (corona) ($1.1 \leq h \leq 100$)
par 8	the the photon index for illuminating power-law spectrum ($1.4 \leq r_{out} \leq 3.3$)
par 9	the luminosity of the source in L_{edd} ($10^{-10} \leq L \leq 10^{10}$)
	negative values changes luminosity to intrinsic to the source
par 10	the ratio of primary to reflected radiation Np:Nr ($1 \leq Np:Nr \leq 10$)
par 11	the density of an acc. disc in units of $10^{15} cm^{-3}$ ($10^{-8} \leq L \leq 10^8$)
par 12	the density profile in Power-law form r^{d_p} ($-5 \leq d_p \leq 0$)
par 13	the abundance of iron relative to solar value ($0.1 \leq$ abundance ≤ 20)
par 14	the redshift of the source ($-0.999 \leq z \leq 10$)
par 15	defines the emission dirrectionality
	1 - isotropic emission (local flux ~ 1)
	2 - Laor's limb darkening (local flux $\sim 1 + 2.06\mu_e$)
	3 - Haardt's limb brightening (local flux $\sim \ln[1 + 1/\mu_e]$)
par 16	defines tables used for reflection
	1 - Older version of reflionx reflection tables
	2 - Updated reflionx reflection tables
	3 - Axisymmetric version of xillver reflection tables is used
par 17	1 - the ionisation parameter is determined by the total incident
	energy flux which is relativistically shifted
	2 - the ionisation parameter is determined by the normalization
	of the incident flux
norm	normalization of the model

Kyconv model parameters

Parameter	Definition and possible values
par 1	the black hole angular momentum in units of GM/c ($0 \leq a/M \leq 1$)
par 2	the observer inclination in degrees (0° - pole, 90° - disc)
par 3	the inner edge of an accretion disc in GM/c^2 ($1 \leq r_{out} \leq 1000$)
par 4	0 - means integration from the disc inner edge, par3
	1 - if par3 is bellow ISCO, integration is done above ISCO only
par 5	the outer edge of an accretion disc in GM/c^2 ($1 \leq r_{out} \leq 1000$)
par 6	the outer power-law index for the radial dependence of the emissivity
	that scales as r^{par6} below the boundary radius, par8 ($-20 \leq q_{out} \leq 20$)
par 7	the inner power-law index for the radial dependence of the emissivity
	that scales as r^{par7} above the boundary radius, par8 ($-20 \leq q_{in} \leq 20$)
par 8	the boundary radius in units of GM/c^2 ($1 \leq r_{br} \leq 1000$)
par 9	the redshift of the source ($-0.999 \leq z \leq 10$)
par 10	defines the emission dirrectionality
	1 - isotropic emission (local flux ~ 1)
	2 - Laor's limb darkening (local flux $\sim 1 + 2.06\mu_e$)
	3 - Haardt's limb brightening (local flux $\sim \ln[1 + 1/\mu_e]$)
par 11	the energy resolution of local flux and resultant spectrum dE
	> 0 relative energy resolution dE/E, the energy grid is equidistant
	in the logarithmic scale
	< 0 absolute energy resolution dE, the energy grid is equidistant
	$= 0$ the data binning is used
par 12	the setting of normalisation of the spectra
	$= 0$ - the total photon flux is the same as the total flux before convolution,
	> 0 - the photon flux at 'par12' keV is the same as the photon flux
	at that energy before convolution,
	$= -1$ - the photon flux is not re-normalised,
	$= -2$ - the maximum of the photon flux is the same as the maximum
	of the photon flux before convolution,
norm	normalisation of the model

Reflionx model parameters

Parameter	Definition and possible values
par 1	the abundance of iron relative to solar value ($0.1 \leq$ Fe ≤ 20)
par 2	the photon index for illuminating power-law spectrum above 0.1 keV ($1.4 \leq$ Gamma ≤ 3.3)
par 3	the ionisation parameter in units erg.cm.s^{-1} ($10 \leq \xi \leq 10000$) defined as $\xi = \frac{4\pi F}{n_H}$ where F - total illuminating flux in 13.6 eV - 13.6 keV and n_H - hydrogen number density
par 4	the redshift of the source
norm	normalization applied to reflected spectrum